ARTICLES
https://doi.org/10.1038/s41556-019-0392-4
nature cell biology

Functional transcription promoters at DNA double-strand breaks mediate RNA-driven phase separation of damage-response factors

Fabio Pessina[1], Fabio Giavazzi[2], Yandong Yin[3], Ubaldo Gioia[1], Valerio Vitelli[1], Alessandro Galbiati[1], Sara Barozzi[1], Massimiliano Garre[1], Amanda Oldani[1], Andrew Flaus[4], Roberto Cerbino[2], Dario Parazzoli[1], Eli Rothenberg[3] and Fabrizio d'Adda di Fagagna[1,5]*

Damage-induced long non-coding RNAs (dilncRNA) synthesized at DNA double-strand breaks (DSBs) by RNA polymerase II are necessary for DNA-damage-response (DDR) focus formation. We demonstrate that induction of DSBs results in the assembly of functional promoters that include a complete RNA polymerase II preinitiation complex, MED1 and CDK9. Absence or inactivation of these factors causes a reduction in DDR foci both in vivo and in an in vitro system that reconstitutes DDR events on nucleosomes. We also show that dilncRNAs drive molecular crowding of DDR proteins, such as 53BP1, into foci that exhibit liquid–liquid phase-separation condensate properties. We propose that the assembly of DSB-induced transcriptional promoters drives RNA synthesis, which stimulates phase separation of DDR factors in the shape of foci.

DNA lesions occur constantly and failure to properly recognize and repair this damage can result in genome instability, cellular senescence or cell death[1,2]. Evolutionarily conserved mechanisms, which are collectively known as the DNA DDR, detect DNA damage, signal its presence and facilitate DNA repair. DNA DSBs are a particularly dangerous class of lesions in which both DNA strands are cleaved[3]. The DDR at DSBs is triggered by recognition of exposed DNA ends by the sensor complex MRE11–RAD50–NBS1 (MRN), which recruits the apical protein kinase ATM to phosphorylate the histone variant H2AX at serine 139, forming γH2AX. This favours the accumulation of several proteins, such as MDC1 and 53BP1, at sites of DNA damage in globular cytologically detectable structures known as DDR foci, in which signalling and repair reactions occur. Recently, we reported that DSBs recruit RNA polymerase II (RNAPII) in a MRN-dependent manner to synthesize dilncRNA that can be processed into shorter DDR RNA (DDRNA), which interacts with DDR factors, such as 53BP1, to accumulate them at DSBs as DDR foci[4–6]. dilncRNA and DDRNA contribute to DNA repair[5,7] and, at resected DNA ends, dilncRNA can form DNA–RNA hybrids that favour DNA repair by homologous recombination[8,9]. We and others have shown that DDR foci disassemble after treatment with RNase A[4,10,11], that RNAPII inhibitors prevent focus formation and DNA repair[5] and that antisense oligonucleotides (ASOs) against dilncRNA and DDRNA generated at individual DSBs can inhibit focus formation and DSB repair in a sequence-specific manner[5]. Despite this evidence, it is unknown whether DSBs recruit factors that are commonly engaged at canonical promoters and whether they are necessary for dilncRNA synthesis and DDR focus formation. Promoters typically recruit machinery comprising RNAPII and six general transcription factor complexes (TFIIA, TFIIB, TFIID, TFIIE, TFIIF and TFIIH), which are collectively known as the preinitiation complex (PIC), although transcription initiation can also occur without canonical promoter sequences[12]. Moreover, studies of the Mediator complex, a transcription coactivator factor that participates in almost all PIC activities, blurred the difference between promoters and enhancers[13–15]. It has recently been reported that the activity of super-enhancers and DNA-binding transcription factors is dependent on liquid–liquid phase separation (LLPS) events[16–20], a process that involves the spontaneous organization of a solution into two phases with different densities[21–24]. RNA is a common agent that is recognized to drive the formation of such biomolecular condensates providing means to compartmentalize and concentrate biochemical reactions[22–28] and multivalent interactions, a feature of RNA, and intrinsically disordered regions of proteins have been proposed to promote LLPS[23,26,29,30]. Furthermore, at sites of DNA damage, some RNA binding proteins have been reported to be rapidly, but transiently, recruited and to undergo liquid demixing promoted by poly(ADP-ribose) (PAR)[31,32]. We therefore tested whether non-coding RNA (ncRNA) generated at DSBs had a role in LLPS leading to DDR focus formation and maturation.

Here we show, both in vivo and in vitro, that general transcription factors that are normally involved at gene promoters in RNAPII regulation are necessary for dilncRNA synthesis at sites of break and that dilncRNAs, together with γH2AX, drive LLPS of DDR factors in the form of DDR foci.

Results

Generation of DSBs leads to the recruitment of the PIC, MED1 and CDK9 together with RNAPII. We previously reported that POLR2A, the catalytic component of RNAPII, is recruited to DNA ends both in vitro in cell extracts and in vivo in cultured cells[5]. To test whether the PIC and associated components MED1 and CDK9 (which we refer to collectively as PMC) are recruited to DSBs

[1]IFOM, The FIRC Institute of Molecular Oncology, Milan, Italy. [2]Dipartimento di Biotecnologie Mediche e Medicina Traslazionale, Università degli Studi di Milano, Segrate, Italy. [3]Department of Biochemistry and Molecular Pharmacology, New York University School of Medicine, New York, NY, USA. [4]Centre for Chromosome Biology, Biochemistry, School of Natural Sciences, National University of Ireland Galway, Galway, Ireland. [5]Istituto di Genetica Molecolare, CNR—Consiglio Nazionale delle Ricerche, Pavia, Italy. *e-mail: fabrizio.dadda@ifom.eu

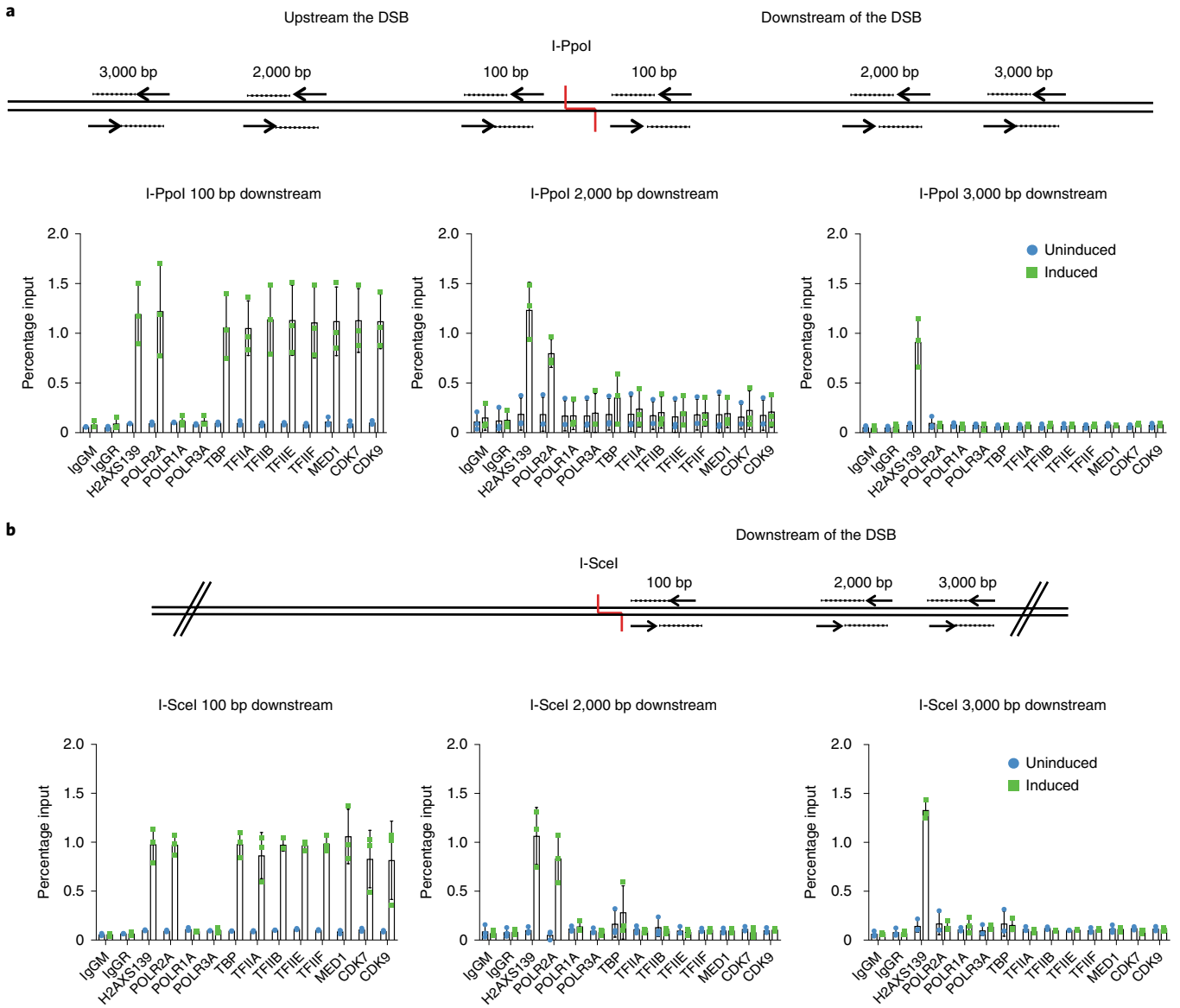

Fig. 1 | RNAPII and PIC are recruited to DSBs, as detected by ChIP in vivo. a, Schematic of the endogenous genomic locus studied. Annealing positions of primer pairs (arrows) used for ChIP–qPCR (amplicons as dotted lines); distances relative to the cut site are indicated. Bar plots show the percentage of enrichment relative to the input of γH2AX, POLR2A, POLR1A, POLR3A, PIC components, MED1 and CDK9 as detected by ChIP at 100 bp, 2,000 bp and 3,000 bp downstream of the DSB (red line) induced by I-PpoI at the DAB1 locus; $n = 3$ independent experiments. **b**, Schematic of the engineered locus studied. Annealing positions of primer pairs used for ChIP–qPCR; distances relative to the cut site are shown. Bar plots show the percentage of enrichment relative to the input of γH2AX, POLR2A, POLR1A, POLR3A, PIC components, MED1 and CDK9 as detected by ChIP at a distance of 100 bp, 2,000 bp and 3,000 bp from the DSB induced by I-SceI at an engineered locus in the HeLa ptight cell line; $n = 3$ independent experiments. Statistics source data are provided in Supplementary Table 2.

in vivo, we performed chromatin immunoprecipitation (ChIP) analyses at an endogenous locus in HeLa cells that can be cleaved by the sequence-specific I-PpoI endonuclease[5], or within a chromosomally integrated artificial construct that can be targeted by I-SceI meganuclease[5]. As a positive control, we used the actin gene promoter (Supplementary Fig. 1a). We mapped the association of the main subunits of PMC and RNAPII by ChIP at 100 bp, 2,000 bp, 3,000 bp from the break before and after DSB induction. γH2AX was detected at all of the sites after DSB. Interestingly, in both systems, all of the tested PMC components and RNAPII were robustly associated at 100 bp from the DSB after its generation. By contrast, at 2,000 bp, only RNAPII was detected, whereas at 3,000 bp, neither PMC nor RNAPII were detectable (Fig. 1a,b, Supplementary Fig. 1b). In a different in vitro system in which DNA oligonucleotides were immobilized on streptavidin beads and incubated with HeLa nuclear extract (Supplementary Fig. 1c), RNAPII (POLR2A), all of the PMC components tested were found to be associated with DNA ends regardless of their structure (3′ or 5′ 10-nucleotide overhangs or blunt; Supplementary Fig. 1c–e).

To test the genome-wide recruitment of PIC and RNAPII, we used super-resolution imaging in cells treated with the DSB-inducing agent neocarzinostatin (NCS). We therefore determined the degree of colocalization between TBP (a component of TFIID) or CDK7 (a component of TFIIH)—the first and last PIC components recruited to transcriptional promoters, respectively[33]—with γH2AX by stochastic optical

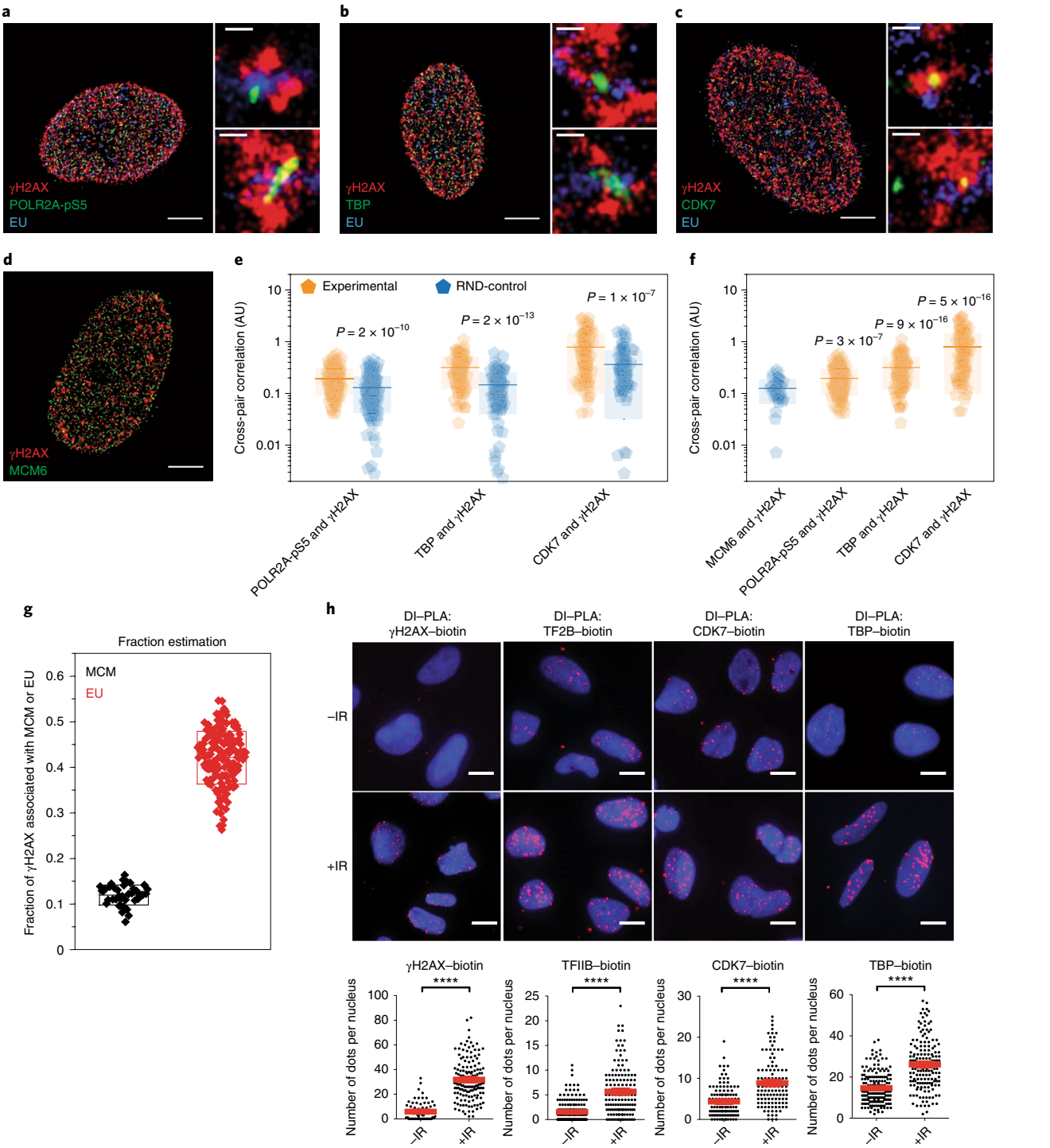

Fig. 2 | RNAP II and PIC components localize to DSB as detected by super-resolution imaging and DI-PLA. a–**c**, Analysis of U2OS cells treated with NCS for 30 min and labelled with EU (15 min pulse) using super-resolution imaging. Representative images of γH2AX and EU stainings with POLR2A-pS5 (**a**) and PIC components TBP (**b**) and CDK7 (**c**). Scale bars, 5,000 nm (left) and 200 nm (right). The experiments were repeated independently 4, 3 and 3 times for **a**–**c**, respectively. **d**, Representative image of γH2AX and MCM6 in a U2OS nucleus treated with NCS for 30 min. Scale bar, 5,000 nm. The experiment was repeated independently twice. **e**,**f**, Statistical analysis of the cross-pair correlation between POLR2A-pS5, TBP or CDK7, and γH2AX, compared with their self-randomized correlation signal (RND-control; **e**), or compared with the correlation between MCM6 and γH2AX (**f**). Data are mean ± s.d.; $n = 184$, $n = 109$, $n = 102$ and $n = 40$ nuclei were collected from 4, 3, 3 and 2 biologically independent experiments for cross-pair correlation analyses between POLR2A-pS5, TBP, CDK7 or MCM and γH2AX, respectively. *P* values were calculated using two-sample unpaired *t*-tests. **g**, The fraction of γH2AX colocalizing with either MCM (black; negative control) or EU (red). Data are mean ± s.d.; $n = 40$ and 162 nuclei collected from 2 and 4 biologically independent experiments for MCM and EU, respectively. $P = 2 \times 10^{-6}$; the statistical analysis was performed using a two-sample unpaired *t*-test. **h**, DI-PLA between biotin and TFIIB, CDK7, TBP or γH2AX in U2OS cells irradiated (2 Gy) and analysed 30 min later or untreated (–IR). Each plot represents at least 80 nuclei analysed. Data are mean ± s.e.m. of $n = 3$ biologically independent experiments. *P* values were calculated using unpaired *t*-tests; $^{*}P < 0.05$, $^{**}P < 0.01$, $^{***}P < 0.001$, $^{****}P < 0.0001$. Representative images are shown; scale bars, 10 μm. Statistics source data are provided in Supplementary Table 2.

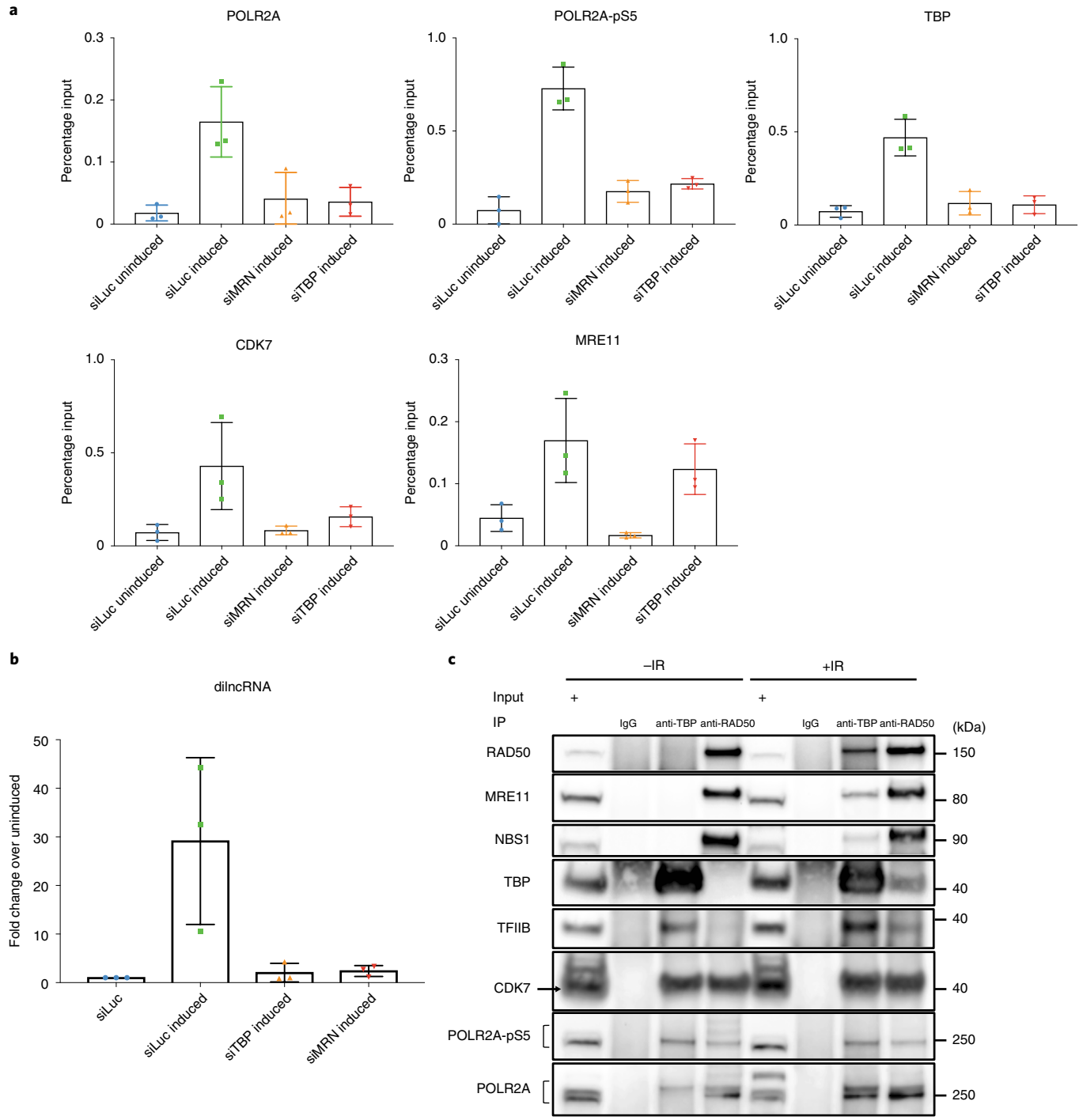

Fig. 3 | MRN complex controls PIC recruitment at endogenous DSB. a, Bar plot shows the percentage of enrichment relative to input of POLR2A, POLR2A-pS5, TBP, CDK7 and MRE11 as detected at the DAB1 locus by ChIP at 100 bp from the DSB induced by I-PpoI in HeLa cells knocked down for MRN (siMRN), TBP (siTBP) or Luciferase (siLuc) as a negative control; $n = 3$ independent experiments. **b**, Induction of diIncRNAs by I-PpoI cut measured by strand-specific qPCR with reverse transcription (RT–qPCR) in HeLa cells knocked down for MRN (siMRN), TBP (siTBP) or Luciferase (siLuc) as a negative control. Bar plots show mean of enrichment of the indicated RNA sets after DSB, relative to uncut; $n = 3$ independent experiments. **c**, Co-immunoprecipitation of TBP and RAD50 following IR exposure. HEK293T cells were irradiated (+IR) or not (−IR) and samples were collected 10 min after IR, followed by immunoprecipitation of individual components of the MRN complex (RAD50) and PIC (TBP). Whole-cell extract (input) and immunoprecipitated samples were analysed by immunoblotting. Mouse immunoglobulin G (IgG) was used as a control. This experiment was repeated twice with similar results. Statistics source data are provided in Supplementary Table 2.

reconstruction microscopy (STORM)[34,35] (Fig. 2a–d). As negative controls, we used both the correlation of signals from two uncorrelated randomly picked nuclei (Fig. 2e), and the correlation between γH2AX and MCM6, which is an abundant DNA replication factor (Fig. 2d,f). As shown in Fig. 2e,f, γH2AX signals colocalized with the active form of POLR2A,

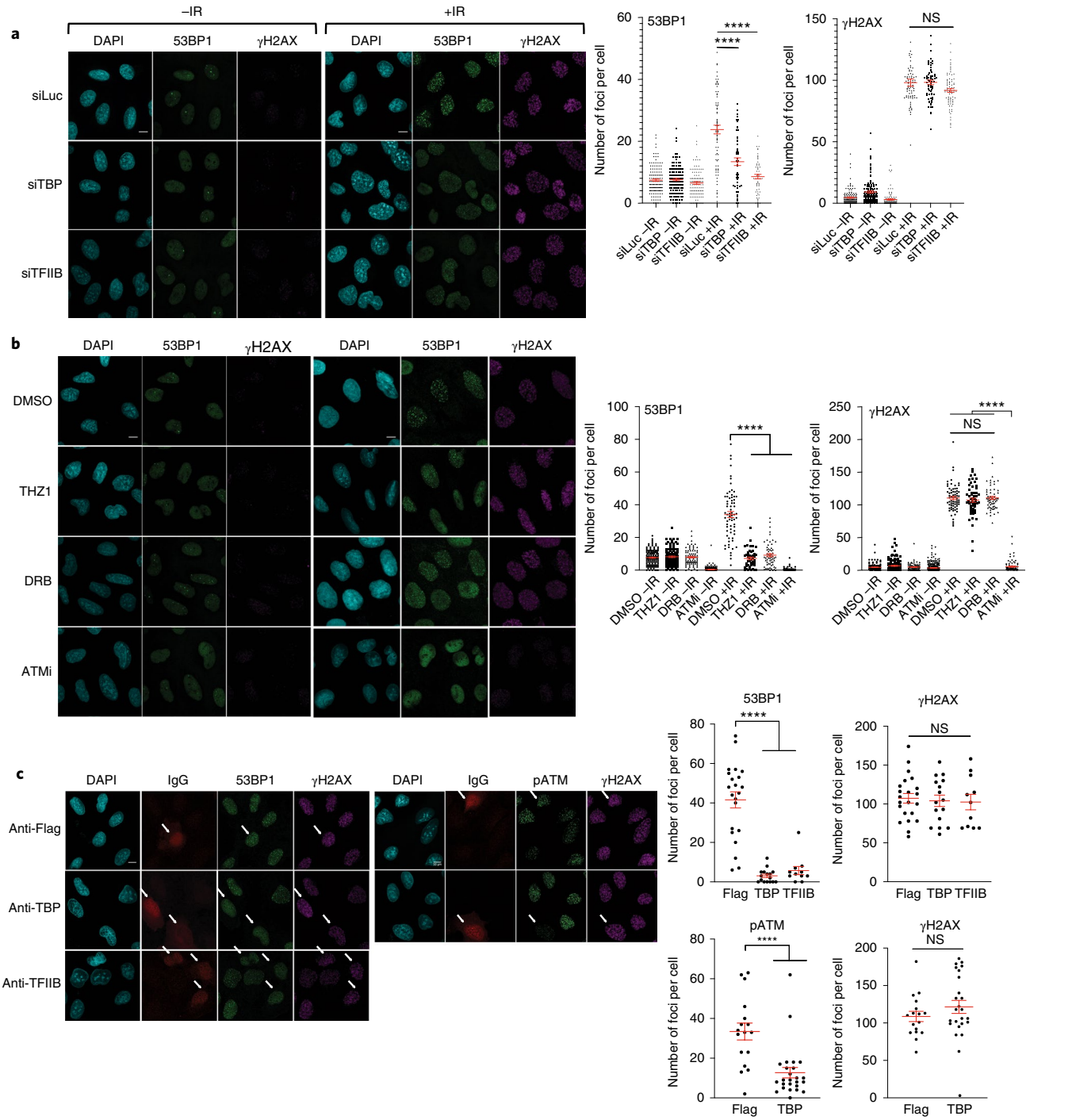

Fig. 4 | PIC inactivation by RNA interference, small molecules or inhibitory antibodies reduces DDR signalling in cultured cells. a, Knockdown of indicated proteins by siRNAs in U2OS cells that were exposed to IR (1 Gy; +IR) or not (−IR), fixed 15 min afterwards and immunostained. Focus formation of the indicated DDR factors were visualized and quantified. Data are mean ± s.e.m. of $n = 131$ siLuc −IR, $n = 131$ siTBP −IR, $n = 108$ siTFIIB −IR, $n = 190$ siLuc +IR, $n = 151$ siTBP +IR and $n = 153$ siTFIIB +IR nuclei analysed from 1 (−IR) or 3 (+IR) biologically independent experiments. γH2AX +IR quantifications are the pool of datasets from **a** and Supplementary Fig. 4a,b. *P* values were calculated using one-way ANOVA. NS, not significant. **b**, U2OS cells treated with dimethyl sulfoxide (DMSO), THZ1, DRB or an ATM inhibitor (ATMi) for 30 min were exposed to IR (1 Gy, +IR) or not (−IR). The cells were fixed and immunostained 15 min after irradiation. Focus formation of indicated DDR factors was visualized and quantified. Data are mean ± s.e.m. of $n = 139$ DMSO −IR, $n = 129$ THZ1 −IR, $n = 84$ DRB −IR, $n = 270$ ATMi −IR, $n = 104$ DMSO +IR, $n = 90$ THZ1 +IR, $n = 117$ DRB +IR and $n = 133$ ATMi +IR nuclei analysed from 1 (−IR) or 2 (+IR) biologically independent experiments. γH2AX +IR quantifications are the pool of datasets from **b** and Supplementary Fig. 4f. *P* values were calculated using one-way ANOVA. **c**, Antibodies against the regulatory domains of TBP or TFIIB were microinjected into the nuclei of U2OS cells (indicated by white arrows); 20 min later, the cells were irradiated (1 Gy) and, after an additional 15 min, the cells were fixed and immunostained. Focus formation of the indicated DDR factors was visualized and quantified in injected cells that were identified by staining against the microinjected antibodies. Data are mean ± s.e.m. of the number of foci per IgG-positive nucleus detected and analysed. *P* values were calculated using unpaired *t*-tests. For the 53BP1 experiment (left) nuclei counts were as follows: Flag, 22 nuclei; TBP, 17 nuclei; and TFIIB, 11 nuclei. For the pATM experiment (right), nuclei counts were as follows: Flag, 17 nuclei; and TBP 25 nuclei. For **a**–**c**, scale bars, 10 μm. Statistics source data are provided in Supplementary Table 2.

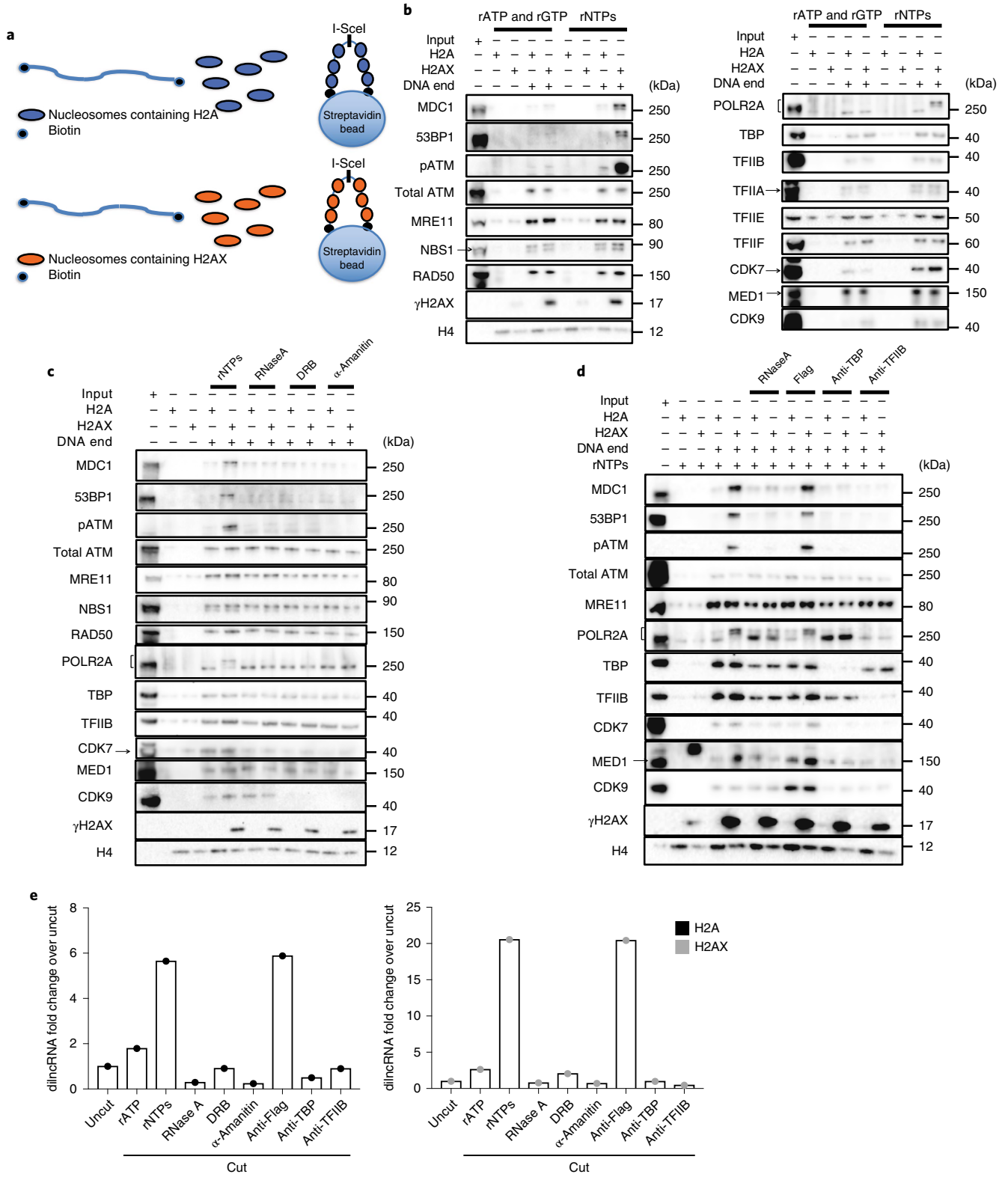

Fig. 5 | An in vitro assay demonstrates a role of the PIC and of RNA synthesis in the recruitment of DDR factors at DSBs. a, Recombinant nucleosomes containing either H2A or H2AX were immobilized on streptavidin beads, either mock treated or cut with I-SceI endonuclease, and then incubated with HeLa nuclear extract. **b**–**d**, Immunoblots of the indicated proteins associated with nucleosomes in different conditions are shown. **b**, Recruitment of DDR factors at chromatinized DSBs assayed in the presence of only rATP and rGTP (no transcription) or in the presence of the full set of rNTPs (transcription allowed). (**c**) Recruitment of DDR factors at chromatinized DSBs assayed after the following treatments: RNA degradation by RNase A, transcription inhibition by DRB and α-amanitin; (**d**) antibodies against the regulatory domains of TBP and TFIIB proteins, or Flag as negative control. In **b**–**d** the experiments were repeated twice with similar results. **e**, One-tenth of the in vitro reactions from panels **b**–**d** was used to measure dilncRNA synthesis by strand-specific RT–qPCR; $n=1$ per experiment. Statistics source data are provided in Supplementary Table 2.

which is phosphorylated at Ser 5 (POLR2A-pS5). Furthermore, we observed significant colocalization of TBP and CDK7 with γH2AX in damaged cells (Fig. 2b,c) and in untreated cells experiencing endogenous low levels of DNA damage (Supplementary Fig. 2a–c,g,h). We also pulsed cells with ethynyl uridine (EU) to detect nascent transcripts following DSB generation. By calculating the correlation in treated versus untreated cells, we confirmed that EU–γH2AX colocalization levels increased in NCS-treated cells proportionally with increased γH2AX signal (Pearson coefficient = 0.31; Supplementary Fig. 2l) and that around 50% of γH2AX signals colocalized with EU (Fig. 2g, Supplementary Fig. 6)—which is probably an underestimation given the 3% substitution rate of uridine with EU[36].

To independently validate the proximity of PIC components to DSB DNA ends, we exploited DNA-damage in situ ligation followed by proximity ligation assay (DI–PLA)[37,38]. DI–PLA confirmed that TBP, TFIIB, CDK7 and γH2AX are all in close proximity to DNA ends in cells exposed to ionizing radiation (IR), whereas the abundant cyclin A is not (Fig. 2h, Supplementary Fig. 2m).

Together, these independent approaches consistently indicate that the PMC components and RNAPII assemble at DSBs and coexist with local RNA synthesis.

RNAPII localization to DSBs is dependent on PIC and MRN. To test the role of the PIC on recruitment or stabilization of RNAPII at DSBs, we knocked down TBP, or MRN as control, using short interfering RNA (siRNA; Supplementary Fig. 3a), and monitored the association of RNAPII with a genomic DSB using ChIP as in Fig. 1a. We observed that accumulation of total and active RNAPII at the DSB was strongly inhibited after TBP knockdown, comparable to MRN loss (Fig. 3a). Similar to their assembly at promoters[33], CDK7 recruitment depends on TBP. TBP and CDK7 also depend on MRN, but not vice versa (Fig. 3a). Knockdown of TBP strongly inhibited dilncRNA synthesis, similarly to MRN inactivation, indicating a crucial role of the components of PIC in dilncRNA synthesis (Fig. 3b).

As PIC recruitment and function is impaired after MRN knockdown, we next tested whether this effect could be mediated by their biochemical interaction. We observed that immunoprecipitation of the MRN complex using antibodies against RAD50 pulled down the PIC components tested as well as RNAPII. At the same time, antibodies against TBP immunoprecipitated MRN in addition to POLR2A. Some interactions were stronger when performed in extracts from irradiated cells (Fig. 3c).

These results are consistent with a model in which MRN acts as a tethering factor at DSBs for PIC, with which it forms a complex. A lack of PIC prevents POLR2A accumulation or retention at DSB and, as a consequence, dilncRNA synthesis.

PIC inactivation by RNA interference, pharmacological inhibition or inhibitory antibodies reduces DDR signalling in cells. To determine the functional contribution of PIC to DDR activation at DSBs, we individually knocked down TBP and TFIIB to prevent PIC assembly and monitored DDR focus formation. We observed that cells with reduced levels of TBP or TFIIB showed reduced 53BP1, phosphorylated ATM (pATM) and formation of MDC1 foci after exposure to IR (Fig. 4a, Supplementary Fig. 4a,b) despite unaltered levels of DDR proteins (Supplementary Fig. 3b). Expression of knockdown-resistant alleles of TBP and TFIIB restored focus formation (Supplementary Fig. 4c). γH2AX focus formation was unaffected in number, with a small reduction in intensity. Consistent with these results, TBP or TFIIB knockdown reduced RNA synthesis at DSBs (Supplementary Figs. 3b and 4d) and of canonical transcription (Supplementary Fig. 4e). As prolonged knockdown of PIC components could alter the expression of cellular genes and have an indirect impact on the DDR, we acutely inhibited PIC functions by treating cells with THZ1, a small-molecule CDK7 inhibitor[39], for 30 min, irradiated the cells and fixed them for immunofluorescence 15 min later. Pharmacological inhibition of CDK7 resulted in a reduction in the number of pATM and 53BP1 foci comparable to that observed in response to an ATM inhibitor (ATMi) and to 5,6-dichloro-1-β-D-ribofuranosylbenzimidazole (DRB), an inhibitor of CDK7 and CDK9 (Fig. 4b, Supplementary Fig. 4f). To independently strengthen our conclusions and further reduce the time between PIC inactivation and the study of its impact on DDR, we inactivated PIC components by nuclear microinjection of antibodies against the regulatory domains of TBP or TFIIB, a validated approach[40,41], or against the Flag epitope as negative control. Cells were microinjected, irradiated 20 min afterwards, and fixed and stained for DDR markers after a further 15 min. We observed that irradiated cells that were microinjected with TBP or TFIIB antibodies showed impaired 53BP1 and pATM focus formation, whereas cells injected with Flag antibodies remained unaffected (Fig. 4c).

Together, these observations—which were generated using three independent strategies—demonstrate that the inactivation of PMC consistently results in diminished activation of the DDR in the form of a reduction in DDR foci.

Accumulation of DDR factors at chromatinized DNA ends in vitro is boosted by PIC-dependent local RNA synthesis. To study the roles of the PIC and transcription in the recruitment and activation of DDR factors at DNA ends in the absence of potential indirect alterations of gene expression, we developed an in vitro system to recapitulate the recruitment of DDR factors at DSBs as observed in living cells. We assembled a DNA fragment with biotin at both ends into nucleosomes using recombinant core-histone octamers containing either histone H2A or H2AX. These chromatinized arrays were immobilized on streptavidin-coated beads and cleaved—or mock treated—by I-SceI, generating DNA fragments with free DNA ends (Fig. 5a). The intact or cleaved bead-bound

Fig. 6 | 53BP1 DDR foci are RNA-dependent liquid–liquid demixed condensates. a, Representative images of FRAP of a 53BP1-GFP focus after 30 min from irradiation (2 Gy; left). Right, FRAP analysis of 53BP1-GFP foci in U2OS cells at different timepoints after IR (2 Gy). Data are mean ± s.d. of $n = 18$ (10–30 min), $n = 10$ (1 h), $n = 8$ (4 h) and $n = 5$ (8 h) nuclei from 2 biologically independent experiments. Statistical analysis was performed using one-way ANOVA; $P < 0.0001$. The mean ± s.d. of mobile fractions are shown for each sample. Scale bars, 5 μm (left) and 1 μm (right). **b**, Representative images of partial FRAP within 53BP1-GFP foci through time; scale bars, 5 μm. The kymographs on the right show internal bleaching and homogeneous internal recovery of a representative bleached focus, vertical scale bars, 4 μm. (i) Time of recovery ± s.d. of internally bleached foci 1 h (10 foci), 4 h (17 foci) and 8 h (11 foci) after irradiation (2 Gy). Indicated *P* values were calculated using unpaired *t*-tests. (ii) Recovery kinetics of the same foci; data were obtained from two biologically independent experiments. Data on bottom right are the mean of mobile fractions ± s.d. for each sample. (iii, iv) 53BP1-GFP foci were analysed in the same conditions as i and ii, but THZ1 100 nM was added 30 min before each timepoint. Data on bottom right in (iv) are mean of mobile fractions ± s.d. for each sample. **c**, U2OS cells expressing 53BP1-GFP were irradiated (2 Gy) and, 30 min after IR, the cells were treated with 50 mM NH_4OAc or 1% 1,6-hexanediol (Hex) and observed by time-lapse live-cell microscopy. Representative screenshots and quantification of 53BP1-GFP foci intensity are shown; scale bars, 5 μm. Data are mean ± 95% confidence interval (CI) of at least three independent experiments; at least 25 nuclei were scored per condition. **d**, U2OS cells expressing 53BP1-GFP were irradiated and, 30 min after IR (2 Gy), the cells were treated with 50 mM NH_4OAc. After 1 min, fresh medium was added and the NH_4OAc was diluted to 10 mM. Representative images are shown; scale bar, 5 μm. The experiment was repeated at least three times with similar results. Statistics source data are provided in Supplementary Table 2.

nucleosomes were incubated with HeLa nuclear extract that was precleared of chromatin and free of rNTPs, therefore making transcription dependent on exogenously added rNTPs. We incubated uncut or cut nucleosome arrays with nuclear extract and rATP and rGTP to provide energy to the system without enabling transcription (Fig. 5b,e). Under these conditions, we observed MRN,

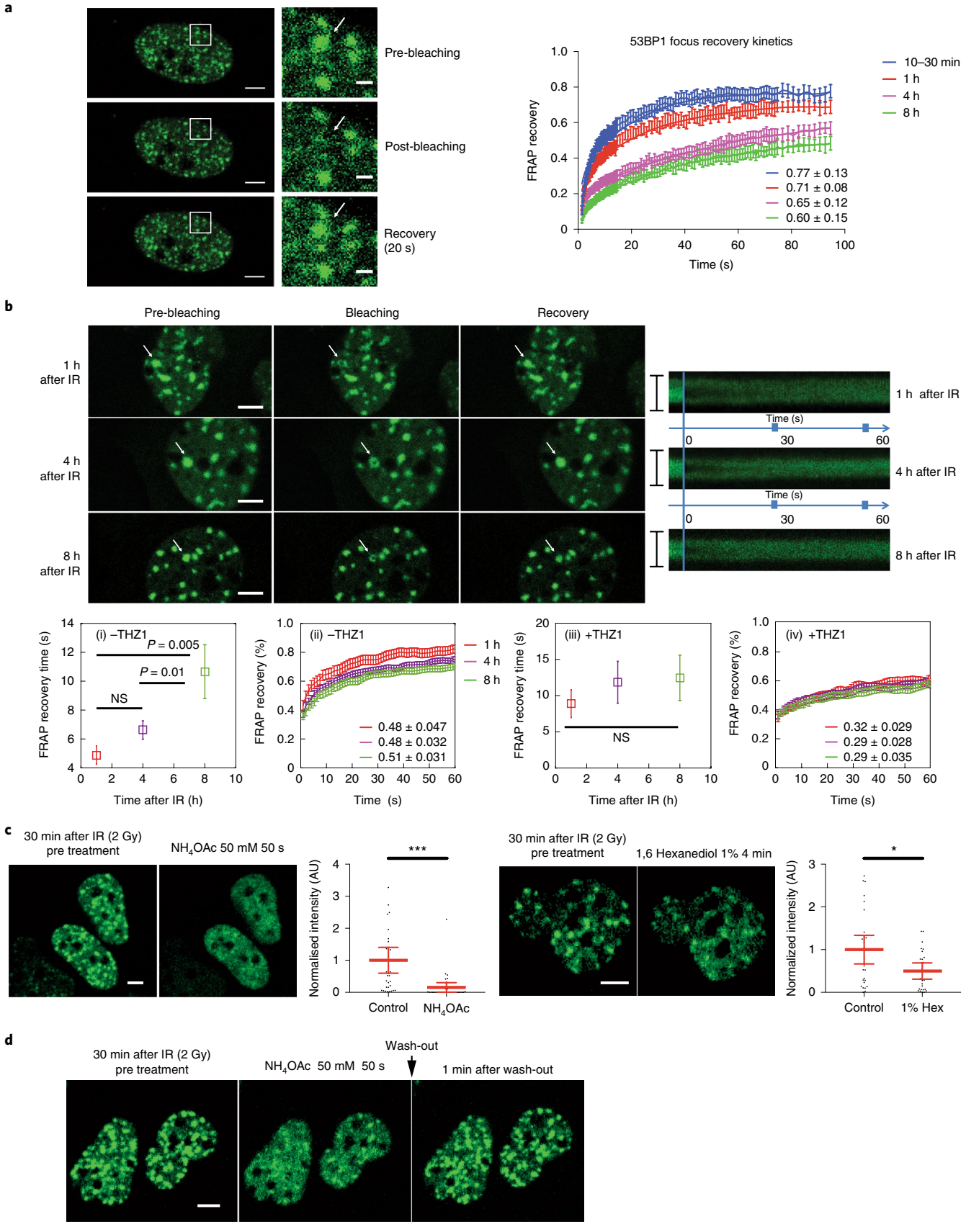

ATM and POLR2A binding as well as PMC accumulation only on chromatin-bearing DNA ends. Despite γH2AX generation, MDC1, 53BP1 or pATM could not be robustly detected in association with cut chromatin. When the complete rNTP pool was supplied and RNA synthesis was enabled (Fig. 5b,e), a strong H2AX-dependent accumulation of MDC1, 53BP1 and pATM was observed on cut nucleosome arrays. The observed accumulation of DDR factors (secondary recruitment), which is not only γH2AX-dependent but also transcription-dependent, is consistent with our observations in cells. Furthermore, as PIC and RNAPII recruitment to cut nucleosomes was independent of RNA synthesis, and rNTPs were necessary for secondary DDR factor recruitment, the contribution of PMC and RNAPII to DDR probably depends on their ability to support RNA synthesis (Fig. 5b,e). To further probe the requirement for RNA synthesis, we treated our reactions with RNase A to degrade RNA, or with DRB or α-amanitin to prevent RNA synthesis (Fig. 5c,e). All three treatments prevented secondary recruitment of DDR factors despite having no impact on γH2AX (Fig. 5c), consistent with results above.

Having validated this system, we used it to test the role of the PIC. We therefore included, in our reactions, inhibitory antibodies raised against the regulatory domains of TBP or TFIIB, or Flag as negative control, as described above in cells (Fig. 4c). We observed that antibodies against TBP or TFIIB prevented recruitment of downstream PMC components, such as CDK7, MED1 and CDK9, to DSBs, and this in turn reduced pATM, 53BP1 and MDC1 recruitment despite unchanged γH2AX levels (Fig. 5d). Furthermore, PIC inhibition reduced dilncRNA levels (Fig. 5e).

In summary, we established and validated an in vitro nucleosome array system that recapitulates tested DDR activation and transcriptional events that occur at DSBs in cells. By exploiting this system, we demonstrated that RNA synthesis, supported by PIC components, is essential for H2AX-dependent recruitment of DDR factors.

53BP1 foci at DSBs show LLPS characteristics. DDR foci are membraneless globular nuclear bodies. The results shown here and those previously published[4,5,11] indicate that the formation of these foci depends on RNA molecules generated at DSBs. Recently, it was shown that a number of intracellular structures are generated by protein LLPS promoted by RNA[22–28]. We therefore hypothesized that PMC-supported RNA synthesis by RNAPII at DSBs could facilitate LLPS of DDR factors in the form of DDR foci. 53BP1 is a major component of DDR foci, the accumulation of which at DSBs has been shown to be dynamic[42] and RNA dependent[4–6,10]. 53BP1 contains both short low-complexity regions and long intrinsically disordered regions (Supplementary Fig. 5a,b), as well as a high content of serine residues and charged regions that are known to facilitate condensate formation[23,24]. A hallmark of liquid-like condensates is a fast and homogeneous internal dynamic reorganization and rapid exchange between phases, which can be observed by fluorescence recovery after photobleaching (FRAP)[23–25]. We therefore used U2OS cells stably expressing near-endogenous levels of 53BP1 fused to green fluorescent protein (GFP)[42] and photobleached individual 53BP1–GFP foci at different timepoints after irradiation to test whether they showed liquid-like behaviours. We observed a fast and homogeneous recovery within 7–20 s comparable to previously reported liquid compartments[17,18,23,43] (Fig. 6a). This behaviour seemed to evolve with time and did not arise from a progressive increase in focus size, as an increase in FRAP recovery time was observed after bleaching only a small area of fixed size at the centre of foci at different timepoints (Fig. 6b, i and ii), confirming a progressive increase in internal viscosity as previously reported for other bodies[23–25,31].

From the diffusion coefficient of 53BP1 molecules within foci, we estimated an average viscosity of 2.5 Pa s (see Methods)—this value, similar to glycerol[44], is 500× greater than that of the nucleoplasm. Recent reports showed that RNA is able to modulate, in a sequence-dependent manner, the viscoelastic properties of condensates and, in particular, to promote a faster exchange rate and prevent fast maturation[45,46]. We therefore tested whether de novo transcription could also be functional in regulating liquid properties of 53BP1 foci. After treatment with THZ1, 53BP1 foci showed considerably slower recovery times in FRAP experiments, suggesting that RNA favours 53BP1 internal mobility and, therefore, liquid-like behaviour (Fig. 6b, iii and iv). Ammonium acetate (NH_4OAc) has been used to target RNA foci [43], and 1,6-hexanediol[47] has been used to perturb liquid-like droplets[48]. After treatment with NH_4OAc, 53BP1 foci completely dissolved within seconds and promptly reformed after wash-out (Fig. 6c,d, Supplementary Video 1); similarly, treatment with 1,6-hexanediol severely reduced the intensity of 53BP1 foci (Fig. 6c).

To determine the biophysical properties of 53BP1 foci, we next performed live-cell analysis of the dynamics and morphology of individual foci after IR. During the first 100 min, the number and average focal radius of detected foci per nucleus increased over time (Fig. 7a, i and ii). Subsequently, a decrease in the total number of foci N_{foci}, but an increase in average focal radius R, were observed owing to the progressive coalescence or ripening of smaller foci (Fig. 7a,b, iii and iv; Supplementary Videos 2 and 3), whereas the total volume of mature 53BP1 foci per nucleus remained constant (Fig. 7a, v). Such a progression of nucleation, growth and coarsening is a characteristic of binary-fluid phase separation with a low-volume fraction in the transformed phase[25,49–51]. The asymptotic behaviours of N_{foci} and R as a function of time can inform the processes that drive coarsening[21,50,52]. The observed combination of $N_{foci} \approx t^{-0.8\pm0.2}$ and $R \approx t^{0.29\pm0.05}$ is compatible with both diffusion-limited coarsening

Fig. 7 | Biophysical properties of 53BP1 condensates. a,**b**, U2OS cells expressing 53BP1–GFP were irradiated (2 Gy) and analysed (more than 20 nuclei from 2 independent experiments) using time-lapse live-cell microscopy for 12 h starting 10 min after IR treatment. **a**, Representative images, captured from Supplementary Video 2, showing the kinetics of 53BP1–GFP focus formation (top, scale bar, 5 μm). Temporal evolution of the average radius of the foci (i). The continuous thin line indicates the best fit to the data using the function $[K(t+t_0)]^n$ with the best fitting exponent being $n = 0.29 \pm 0.05$, compatible with the value 1/3 expected in both DLC and BMC scenarios. Temporal evolution of the average number of foci per nucleus (ii). Probability distribution function PDF(R) of foci radius measured at different timepoints (logarithmically spaced between 1 min and 700 min) (iii). PDF(R) (iv) as in (iii), with both axes rescaled with the average radius $\langle R \rangle$. A collapse of all of the curves onto an invariant distribution is observed for $t > 100$ min. Temporal evolution of the total volume of foci per nucleus (estimated as $\frac{4}{3}\pi N_{foci}\langle R \rangle^3$) (v). Schematic of the proposed model of 53BP1 foci kinetic through LLPS (vi). **b**, Example of coalescence of 53BP1 foci (top) and the associated kymographs (bottom, vertical scale bars, 4 μm). **c**, 53BP1–GFP U2OS cells were treated and analysed as in **a** (i–v) but, 30 min after IR, THZ1 100 nM was added. **d**, Decorrelation rate $\Gamma(q)$ obtained from Fourier analysis of droplet shape fluctuations as a function of the wave vector q (i; Supplementary Fig. 6c). $\Gamma(q)$ follows the dispersion relation expected for overdamped capillary waves and provides an estimate of the propagation speed $v_0 = 0.45 \pm 0.1\,\mu m\,s^{-1}$. Characteristic lifetime τ of shape fluctuations as a function of the foci size as obtained from intensity correlation analysis (ii). Each red or blue circle corresponds to one focus measured 4 h or 8 h after irradiation, respectively ($n = 51$ foci). Black boxes: average τ calculated by binning the data over intervals of width 0.05 μm, bars: associated standard error. **e**,**f**, Average intensity and volume of 53BP1–GFP single foci after treatment with sequence-specific ASOs and control ASOs (control). **e**, The transfection experiment was repeated twice with similar results. **f**, The microinjection experiment was repeated four times with similar results. Statistics source data are provided in Supplementary Table 2.

(DLC) and Brownian-motion coalescence (BMC) [21,50,52]. However, the majority of droplets disappear without physical contact, suggesting that DLC could be the dominant process (Fig. 7a, vi). Another characteristic of liquid–liquid interfaces is surface-tension-driven fluctuations (capillary waves)[53]. Measurements of spontaneous shape fluctuations of 53BP1 foci (Supplementary Fig. 5c, i–iii) were consistent with capillary waves in an overdamped regime[54] (Fig. 7d, i). The characteristic lifetime τ of the shape fluctuations scales linearly with the size R of 53BP1 foci: $\tau \approx R$ (Fig. 7d, ii), strongly supporting a model of shape fluctuations due to capillary waves on the surface of a viscous droplet[55], with $c \approx \eta/\gamma$. Combining our estimates of internal viscosity η and fluctuation lifetime, we calculated that the effective surface tension of 53BP1 foci is very low: $\gamma \approx 0.5\,\mu N\,m^{-1}$, similar to that of P granules[56].

We next tested whether inhibition of dilncRNA could affect this progression. We observed that 53BP1 foci progression was

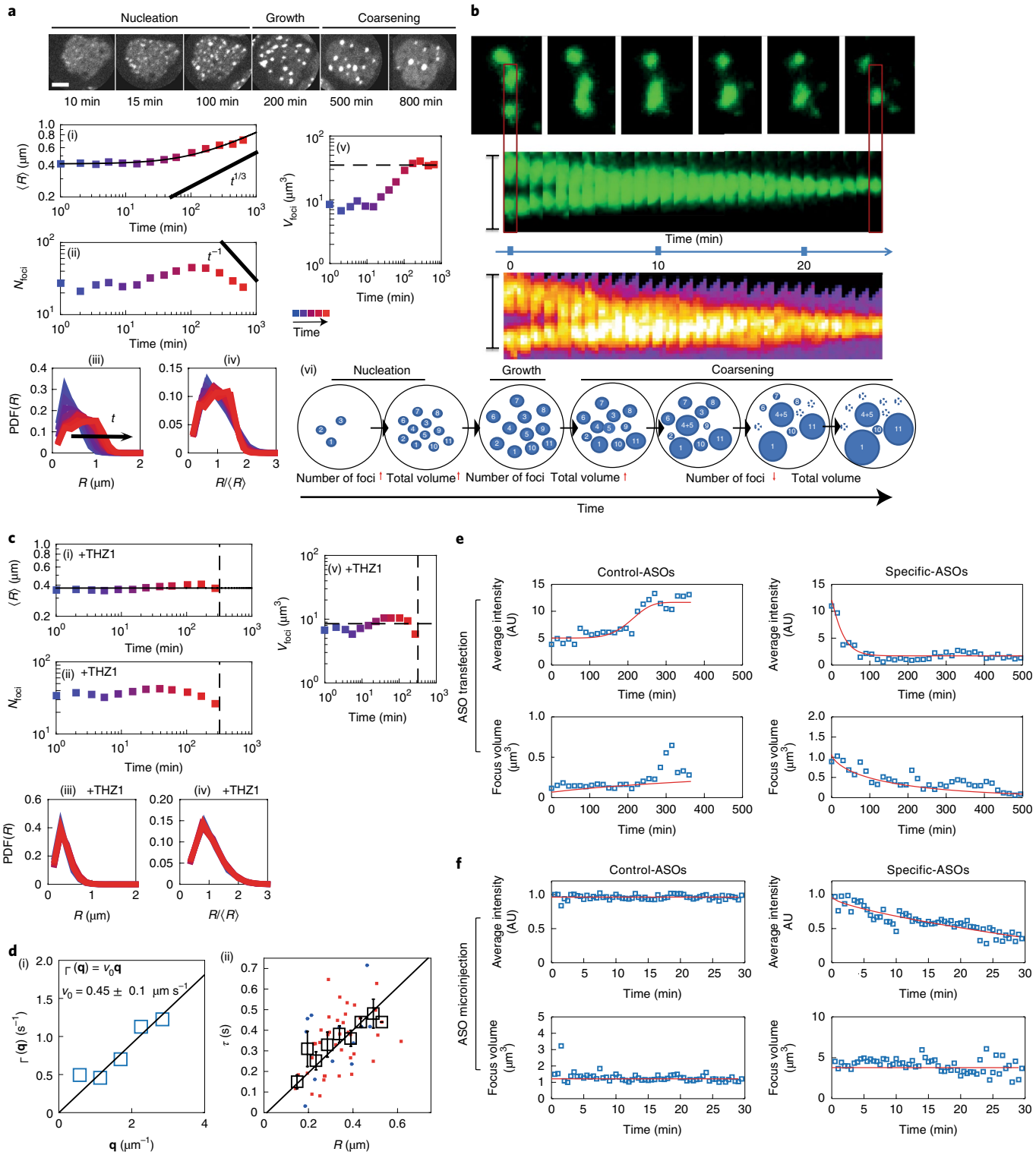

halted by transcription inhibition, with foci maturation arrested during the nucleation phase (when treatment started) and the foci were unable to enter the growth and coalescence phase (Fig. 7c and Supplementary Video 4), indicating that de novo transcription regulates the physical properties of 53BP1 foci throughout their temporal evolution. Moreover, we tested the impact of ASOs on the formed 53BP1 foci. Both lipofection and microinjection of sequence-specific ASOs against dilncRNA (but not control-ASOs) in NIH 2/4 cells, in which DSB can be induced at a known and traceable locus[5], caused the 53BP1 focus to disappear (Fig. 7e,f and Supplementary Video 6). We next studied whether foci were disappearing as solid or liquid objects. By measuring the volume of the imaged 53BP1 foci and their average intensity after ASO treatment, as a measure of their density, we observed a decrease in average intensity during a timescale that was 10× faster than that associated with size reduction (Fig. 7e,f). This biophysical behaviour is typical of liquid/viscous objects and not of solid ones.

Overall, these results are consistent with the 53BP1 foci being LLPS compartments dependent on dilncRNA through time.

RNA synthesis drives phase separation of 53BP1 at DSB in vitro. To further investigate the contribution of RNA to 53BP1 focus formation by LLPS, we used the in vitro system described above (Fig. 5a–d) with nuclear extracts from cells expressing 53BP1–GFP[42]. In the reactions containing H2AX supplemented with the full set of rNTPs or cellular RNA we noted that the solutions turned opaque (Supplementary Fig. 5d). To test whether this increase in turbidity, which is often indicative of macromolecular phase transition, was due to droplet formation, we analysed the solutions using differential interference contrast (DIC) microscopy and fluorescence microscopy. We observed that only the combination of H2AX-containing nucleosome arrays and rNTPs enabled the formation of 53BP1–GFP-containing condensates (Fig. 8a). Photobleaching of these condensates resulted in rapid and homogeneous liquid-like recovery (Fig. 8b) and addition of NH_4OAc disrupted them (Fig. 8a), supporting their nature as liquid compartments. Notably, although cellular RNA favoured droplet formation, the formed droplets were not 53BP1–GFP positive, demonstrating that cellular transcripts that were not generated from H2AX-containing nucleosomes templates did not make a significant contribution to the formation of 53BP1 condensates in this system (Fig. 8a). To further validate our in vivo observations on the role of PIC components and dilncRNAs, we tested the impact of transcriptional inhibitors or ASOs against dilncRNA, or the impact of antibodies against TBP and TFIIB. We observed that all of these treatments prevented the formation of 53BP1–GFP droplets (Fig. 8c) and transcriptional inhibitors or ASOs also disrupted the droplets once they were already formed (Fig. 8d). We therefore demonstrated, in a controlled in vitro system, a role for PIC components and dilncRNA in promoting 53BP1 LLPS events.

Phase separation and de novo transcription impact DSB repair. We previously reported that transcription inhibition or ASOs against dilncRNA impair DSB repair[5]. To test the role of PIC components and LLPS events in DNA repair, we studied the impact of transcription inhibition by THZ1 and of phase separation disruption by ammonium acetate (NH_4OAc)[43] on DSB repair in irradiated HeLa cells by neutral comet assay; mirin, a MRN inhibitor[57], was used as a control. All of these treatments resulted in increased comet tail moment, which is indicative of impaired DNA repair (Fig. 8e). Furthermore, we used EJ5–GFP U2OS cells[58] to monitor the effects of transcription or LLPS impairment on DNA repair through distal non-homologous end joining, a pathway in which 53BP1 plays a key role[59]. By measuring the religation rates following the generation of two distant DSB[7] using genomic DNA quantitative PCR (qPCR), we observed a clear reduction in the efficiency of DNA repair in cells treated with the CDK7 inhibitor THZ1 or the LLPS inhibitor 1,6-hexanediol (Fig. 8f). Impairment of DNA repair was comparable to MRN inhibition by mirin, with the only difference being that mirin was highly toxic in cut cells at day two.

Overall, these results show that PIC components and LLPS positively contribute to DSB repair.

Discussion

The DDR, including DNA-damage signalling and repair, has been shown to be regulated by RNA in several independent reports[60], but the mechanisms of RNA synthesis—including the proteins involved and whether these mechanisms are unique to DSB or shared with other transcriptional apparatuses—has remained unclear. Here we show that DSBs recruit the main subunits of the PIC and Mediator complexes and elongation factor CDK9. Our results suggest a model in which MRN recognizes DNA ends and recruits the PIC and Mediator complexes which, together with CDK9, promote the full activation of POLR2A. Inactivation of PIC components prevents RNAPII detection and transcription at DSB sites, impairing signalling and repair. Our results, supporting a linear cascade of events in which MRN recruits PIC that recruits RNAPII, may also be compatible with PIC and RNAPII mutually stabilizing each other at DSBs in an MRN-dependent manner. Either way, DSBs serve as sites of sequence-independent recruitment of transcriptional activity that is reminiscent of transcriptional promoters or enhancers. Importantly, the function of the PIC in the DDR depends on its ability to fuel dilncRNA synthesis at DNA breaks, as demonstrated in our in vitro system.

The notion that PIC components are recruited at DSBs and that they are essential for full DDR activation by promoting RNA

Fig. 8 | 53BP1 forms droplets in vitro in a transcription-dependent manner and 53BP1 LLPS is important for DSB repair in cells. a, Representative images of droplet formation in U2OS 53BP1-GFP nuclear extracts (NE). Both DIC and GFP (fluorescein isothiocyanate; FITC) channels are shown. The experiment was repeated twice with similar results. **b**, FRAP of the internal fraction of a 53BP1-GFP condensate and images of recovery are shown. The experiment was repeated twice with similar results. **c**, Representative images of droplet formation in U2OS 53BP1-GFP nuclear extracts. H2AX-containing nucleosomes and rNTPs were added to nuclear extract, and reactions were immediately treated as indicated. Both DIC and GFP (FITC) channels are shown; $n=1$. **d**, Representative images of droplet formation in U2OS 53BP1-GFP nuclear extract treated as indicated. H2AX-containing nucleosomes and rNTPs were added to nuclear extract and, after droplet formation, reactions were treated as indicated. Both DIC and GFP (FITC) channels are shown; $n=1$. **e**, DNA repair kinetics were monitored by neutral comet assay at different timepoints after IR (5 Gy) in HeLa cells. Non-irradiated (NI) cells treated with the drugs for 5 h (300 min; asterisk) and untreated control cells (control) are also shown. The dot plot shows quantification of IR-induced DSBs by tail-moment analysis. The red bars indicate mean ± 95% CI of control NI $n=116$, 10 min $n=113$, 300 min $n=114$, NH_4OAc NI $n=69$, 10 min $n=88$, 300 min $n=108$; mirin NI $n=50$, 10 min $n=89$, 300 min $n=71$; THZ1 NI $n=54$, 10 min $n=61$, 300 min $n=70$ cells per sample from three independent experiments. **f**, EJ5-GFP U2OS cells were transfected with a plasmid expressing I-SceI or with an empty vector (EV) and was concomitantly treated with the indicated drugs. Untreated cells (control) were used as a control. DSB rejoining events were evaluated using qPCR (EJ5-GFP) on genomic DNA collected at 24 h or 48 h after plasmid transfection; β-actin was used as a reference. Repair efficiency is shown relative to untreated cells transfected with the EV. Data are mean ± s.e.m. of $n=3$ independent experiments. For **e** and **f**, *P* values were calculated using one-way ANOVA. For **a** and **b**, scale bars, 10 μm; for **c** and **d**, scale bars, 5 μm. Statistics source data are provided in Supplementary Table 2.

synthesis at DSBs may have important consequences beyond mechanistic studies. CDK7 kinase inhibitors such as THZ1 are presently considered to be cancer-therapy candidates[39,61,62], and our results suggest that at least part of the effects of THZ1 on cancer cells, which tend to accumulate high levels of endogenous DNA damage[63], may be related to its impact on DDR.

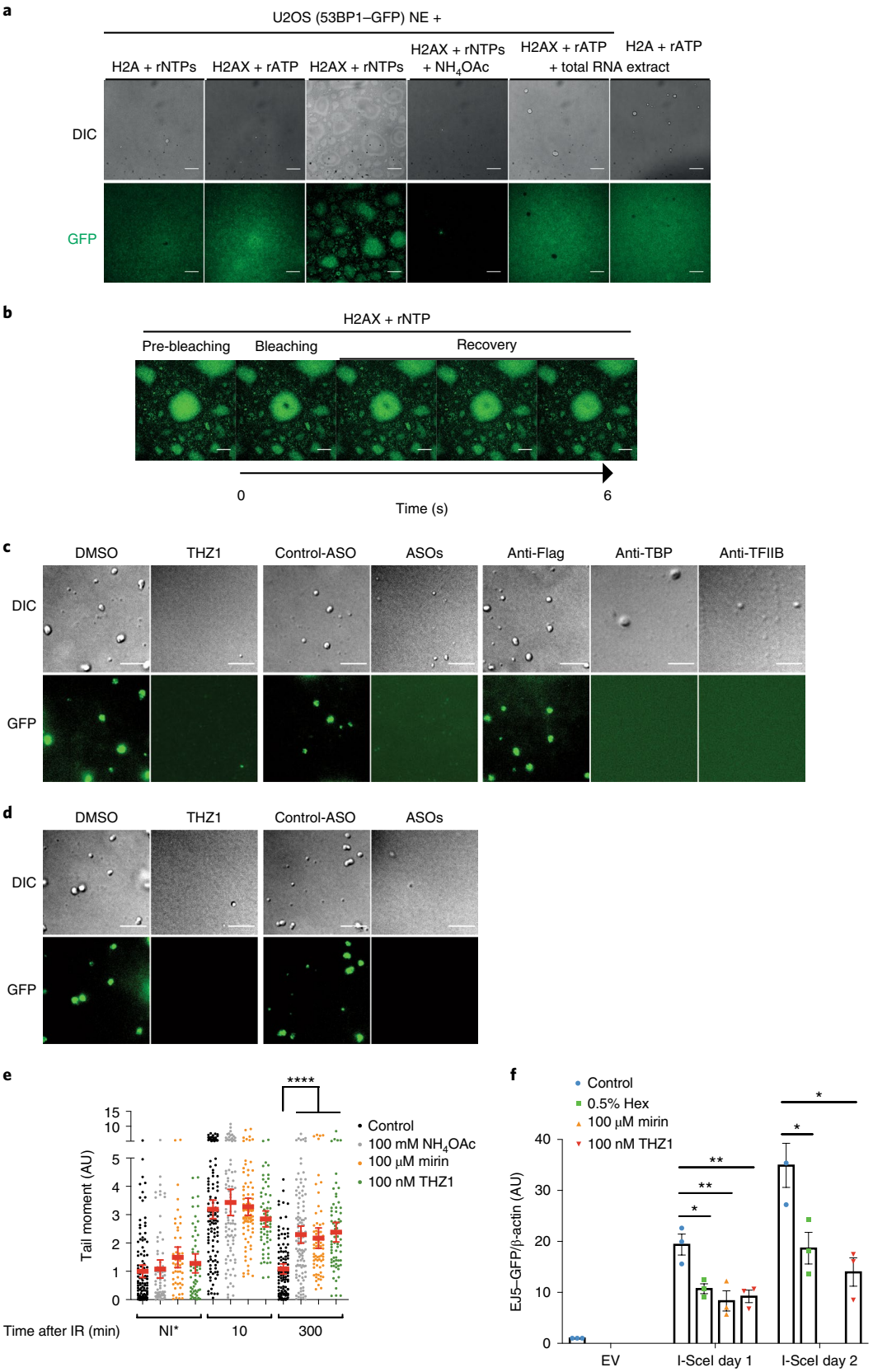

How RNA transcribed from a damaged DNA template contributes to the secondary recruitment of DDR factors has been unclear since its discovery. Here we show that such RNA favours LLPS of the DDR foci component 53BP1. RNA has been shown to function as a driving agent for protein condensation by promoting local concentration of RNA-interacting proteins[30], which can form liquid droplets through liquid–liquid demixing by phase separation. This event probably favours DNA-damage signalling and repair events by controlling diffusion and concentration of DDR factors in proximity to DSBs. Notably, although neither RNA nor γH2AX are sufficient to enable the formation of DDR foci alone, it is possible that γH2AX acts as a beacon recruiting DDR factors by protein–protein interactions[3] and RNA retains them at DSBs through a web of multivalent low-specificity interactions, which may also induce structural changes that favour phase transition and condensate formation. A dynamic behaviour for DDR foci was previously reported[42,64,65]. We now show that DDR foci exhibit liquid-like behaviours, including nucleation, growth and coarsening, that are equivalent to phase-separating fluids; behaving as viscous structures with spontaneous shape fluctuations set by an effective surface tension, DDR foci show rapid recovery from photobleaching, and are sensitive to agents that perturb liquid-like structures. By inhibiting transcription before or during LLPS formation at DSBs, we concluded that RNA synthesis promotes faster molecular exchange and, therefore, fluidity of 53BP1 compartments and controls their evolution in time. Our results are consistent with reports on the emerging role of RNA in preventing increase in gelation of phase-separated bodies[45,46]. In particular, maturation or hardening is typical of IDR-based condensates that, although initially fluid, may become more viscoelastic over time, eventually behaving as solids[24]. Although our experiment with ASOs support a crucial role for dilncRNA in promoting the formation and evolution of 53BP1 condensates, it is possible that they contribute in more than one way to LLPS at DSBs. Indeed, DSB recruitment of RNF168 ubiquitin ligase is dependent on transcription[5], and ubiquitin has been shown to promote[66] and be promoted[67] by phase separation. Moreover, the RNA binding protein FUS undergoes LLPS at DNA-damage sites[31,68], and is dependent on PAR polymers[32], which, to be noted, are markedly similar to RNA. PAR chains may contribute transiently to stabilizing the transcription machinery at DSBs, as suggested previously in other contexts[69]. After a revised version of this manuscript was submitted, a study was published describing LLPS of 53BP1 (ref. [70])

Of note, LLPS may exert roles beyond focus formation, and the reported ability of condensates to exert mechanical forces[71], together with our observed recruitment of MED1 at DSBs, is intriguing and may suggest events similar to those reported at enhancers, also shown to engage LLPS[17,20,46] where distant genetic elements are brought into close proximity.

Online content

Any methods, additional references, Nature Research reporting summaries, source data, statements of code and data availability and associated accession codes are available at https://doi.org/10.1038/s41556-019-0392-4.

Received: 9 January 2019; Accepted: 16 August 2019;
Published online: 30 September 2019

References

1. Jackson, S. P. & Bartek, J. The DNA-damage response in human biology and disease. *Nature* **461**, 1071–1078 (2009).
2. d'Adda di Fagagna, F. Living on a break: cellular senescence as a DNA-damage response. *Nature Rev. Cancer* **8**, 512–522 (2008).
3. Ciccia, A. & Elledge, S. J. The DNA damage response: making it safe to play with knives. *Mol. Cell* **40**, 179–204 (2010).
4. Francia, S. et al. Site-specific DICER and DROSHA RNA products control the DNA-damage response. *Nature* **488**, 231–235 (2012).
5. Michelini, F. et al. Damage-induced lncRNAs control the DNA damage response through interaction with DDRNAs at individual double-strand breaks. *Nat. Cell Biol.* **19**, 1400–1411 (2017).
6. Francia, S., Cabrini, M., Matti, V., Oldani, A. & d'Adda di Fagagna, F. DICER, DROSHA and DNA damage response RNAs are necessary for the secondary recruitment of DNA damage response factors. *J. Cell Sci.* **129**, 1468–1476 (2016).
7. Gioia, U. et al. Pharmacological boost of DNA damage response and repair by enhanced biogenesis of DNA damage response RNAs. *Sci. Rep.* **9**, 6460 (2019).
8. D'Alessandro, G. et al. BRCA2 controls DNA:RNA hybrid level at DSBs by mediating RNase H2 recruitment. *Nat. Commun.* **9**, 5376 (2018).
9. Lu, W. T. et al. Drosha drives the formation of DNA:RNA hybrids around DNA break sites to facilitate DNA repair. *Nat. Commun.* **9**, 532 (2018).
10. Pryde, F. et al. 53BP1 exchanges slowly at the sites of DNA damage and appears to require RNA for its association with chromatin. *J. Cell Sci.* **118**, 2043–2055 (2005).
11. Rossiello, F. et al. DNA damage response inhibition at dysfunctional telomeres by modulation of telomeric DNA damage response RNAs. *Nat. Commun.* **8**, 13980 (2017).
12. Haberle, V. & Stark, A. Eukaryotic core promoters and the functional basis of transcription initiation. *Nat. Rev. Mol. Cell Biol.* **19**, 621–637 (2018).
13. Andersson, R., Sandelin, A. & Danko, C. G. A unified architecture of transcriptional regulatory elements. *Trends Genet.* **31**, 426–433 (2015).
14. Kornberg, R. The molecular basis of eukaryotic transcription (Nobel Lecture). *Angew. Chem. Int. Edn* **46**, 6956–6965 (2007).
15. Vernimmen, D. & Bickmore, W. A. The hierarchy of transcriptional activation: from enhancer to promoter. *Trends Genet.* **31**, 696–708 (2015).
16. Lu, H. et al. Phase-separation mechanism for C-terminal hyperphosphorylation of RNA polymerase II. *Nature* **558**, 318–323 (2018).
17. Sabari, B. R. et al. Coactivator condensation at super-enhancers links phase separation and gene control. *Science* **361**, eaar3958 (2018).
18. Cho, W. K. et al. Mediator and RNA polymerase II clusters associate in transcription-dependent condensates. *Science* **361**, 412–415 (2018).
19. Boehning, M. et al. RNA polymerase II clustering through carboxy-terminal domain phase separation. *Nat. Struct. Mol. Biol.* **25**, 833–840 (2018).
20. Boija, A. et al. Transcription factors activate genes through the phase-separation capacity of their activation domains. *Cell* **175**, 1842–1855 (2018).
21. Berry, J., Weber, S. C., Vaidya, N., Haataja, M. & Brangwynne, C. P. RNA transcription modulates phase transition-driven nuclear body assembly. *Proc. Natl Acad. Sci. USA* **112**, E5237–E5245 (2015).
22. Boeynaems, S. et al. Protein phase separation: a new phase in cell biology. *Trends Cell Biol.* **28**, 420–435 (2018).
23. Shin, Y. & Brangwynne, C. P. Liquid phase condensation in cell physiology and disease. *Science* **357**, eaaf4382 (2017).
24. Banani, S. F., Lee, H. O., Hyman, A. A. & Rosen, M. K. Biomolecular condensates: organizers of cellular biochemistry. *Nat. Rev. Mol. Cell Biol.* **18**, 285–298 (2017).
25. Hyman, A. A., Weber, C. A. & Julicher, F. Liquid-liquid phase separation in biology. *Annu. Rev. Cell Dev. Biol.* **30**, 39–58 (2014).
26. Kato, M. et al. Cell-free formation of RNA granules: low complexity sequence domains form dynamic fibers within hydrogels. *Cell* **149**, 753–767 (2012).
27. Hnisz, D., Shrinivas, K., Young, R. A., Chakraborty, A. K. & Sharp, P. A. A phase separation model for transcriptional control. *Cell* **169**, 13–23 (2017).
28. Langdon, E. M. et al. mRNA structure determines specificity of a polyQ-driven phase separation. *Science* **360**, 922–927 (2018).
29. Li, P. et al. Phase transitions in the assembly of multivalent signalling proteins. *Nature* **483**, 336–340 (2012).
30. Lin, Y., Protter, D. S., Rosen, M. K. & Parker, R. Formation and maturation of phase-separated liquid droplets by RNA-binding proteins. *Mol. Cell* **60**, 208–219 (2015).
31. Patel, A. et al. A liquid-to-solid phase transition of the ALS protein FUS accelerated by disease mutation. *Cell* **162**, 1066–1077 (2015).
32. Altmeyer, M. et al. Liquid demixing of intrinsically disordered proteins is seeded by poly(ADP-ribose). *Nat. Commun.* **6**, 8088 (2015).
33. Lee, T. I. & Young, R. A. Transcription of eukaryotic protein-coding genes. *Annu. Rev. Genet.* **34**, 77–137 (2000).
34. Rust, M. J., Bates, M. & Zhuang, X. Sub-diffraction-limit imaging by stochastic optical reconstruction microscopy (STORM). *Nat. Methods* **3**, 793–795 (2006).
35. Sengupta, P. et al. Probing protein heterogeneity in the plasma membrane using PALM and pair correlation analysis. *Nat. Methods* **8**, 969–975 (2011).
36. Jao, C. Y. & Salic, A. Exploring RNA transcription and turnover in vivo by using click chemistry. *Proc. Natl Acad. Sci. USA* **105**, 15779–15784 (2008).
37. Galbiati, A., Beausejour, C. & d'Adda di Fagagna, F. A novel single-cell method provides direct evidence of persistent DNA damage in senescent cells and aged mammalian tissues. *Aging Cell* **16**, 422–427 (2017).
38. Galbiati, A. & d'Adda di Fagagna, F. in *Cellular Senescence: Methods and Protocols* (ed. Demaria, M.) 11–20 (Springer, 2019).

39. Wang, Y. et al. CDK7-dependent transcriptional addiction in triple-negative breast cancer. *Cell* **163**, 174–186 (2015).
40. Lee, K. B., Wang, D., Lippard, S. J. & Sharp, P. A. Transcription-coupled and DNA damage-dependent ubiquitination of RNA polymerase II in vitro. *Proc. Natl Acad. Sci. USA* **99**, 4239–4244 (2002).
41. Radebaugh, C. A. et al. TATA box-binding protein (TBP) is a constituent of the polymerase I-specific transcription initiation factor TIF-IB (SL1) bound to the rRNA promoter and shows differential sensitivity to TBP-directed reagents in polymerase I, II, and III transcription factors. *Mol. Cell Biol.* **14**, 597–605 (1994).
42. Bekker-Jensen, S., Lukas, C., Melander, F., Bartek, J. & Lukas, J. Dynamic assembly and sustained retention of 53BP1 at the sites of DNA damage are controlled by Mdc1/NFBD1. *J. Cell Biol.* **170**, 201–211 (2005).
43. Jain, A. & Vale, R. D. RNA phase transitions in repeat expansion disorders. *Nature* **546**, 243–247 (2017).
44. Liang, L., Wang, X., Xing, D., Chen, T. & Chen, W. R. Noninvasive determination of cell nucleoplasmic viscosity by fluorescence correlation spectroscopy. *J. Biomed. Opt.* **14**, 024013 (2009).
45. Elbaum-Garfinkle, S. et al. The disordered P granule protein LAF-1 drives phase separation into droplets with tunable viscosity and dynamics. *Proc. Natl Acad. Sci. USA* **112**, 7189–7194 (2015).
46. Nair, S. J. et al. Phase separation of ligand-activated enhancers licenses cooperative chromosomal enhancer assembly. *Nat. Struct. Mol. Biol.* **26**, 193–203 (2019).
47. Kroschwald, S., Maharana, S. & Simon, A. Hexanediol: a chemical probe to investigate the material properties of membrane-less compartments. *Matters* **3**, e201702000010 (2017).
48. Strom, A. R. et al. Phase separation drives heterochromatin domain formation. *Nature* **547**, 241–245 (2017).
49. Onuki, A. *Phase Transition Dynamics* (Cambridge Univ. Press, 2002).
50. Voorhees, P. W. Ostwald ripening of two-phase mixtures. *Annu. Rev. Mater. Sci.* **22**, 197–215 (1992).
51. Zwicker, D., Decker, M., Jaensch, S., Hyman, A. A. & Julicher, F. Centrosomes are autocatalytic droplets of pericentriolar material organized by centrioles. *Proc. Natl Acad. Sci. USA* **111**, E2636–E2645 (2014).
52. Berry, J., Brangwynne, C. P. & Haataja, M. Physical principles of intracellular organization via active and passive phase transitions. *Rep. Prog. Phys.* **81**, 046601 (2018).
53. Caragine, C. M., Haley, S. C. & Zidovska, A. Surface fluctuations and coalescence of nucleolar droplets in the human cell nucleus. *Phys. Rev. Lett.* **121**, 148101 (2018).
54. Jeng, U.-S., Esibov, L., Crow, L. & Steyerl, A. Viscosity effect on capillary waves at liquid interfaces. *J. Phys. Condens. Matter* **10**, 4955 (1998).
55. Gang, H., Krall, A. H. & Weitz, D. A. Shape fluctuations of interacting fluid droplets. *Phys. Rev. Lett.* **73**, 3435–3438 (1994).
56. Brangwynne, C. P. et al. Germline P granules are liquid droplets that localize by controlled dissolution/condensation. *Science* **324**, 1729–1732 (2009).
57. Dupre, A. et al. A forward chemical genetic screen reveals an inhibitor of the Mre11–Rad50–Nbs1 complex. *Nat. Chem. Biol.* **4**, 119–125 (2008).
58. Gunn, A. & Stark, J. M. I-SceI-based assays to examine distinct repair outcomes of mammalian chromosomal double strand breaks. *Methods Mol. Biol.* **920**, 379–391 (2012).
59. Difilippantonio, S. et al. 53BP1 facilitates long-range DNA end-joining during V(D)J recombination. *Nature* **456**, 529–533 (2008).
60. Michelini, F. et al. From "cellular" RNA to "smart" RNA: multiple roles of RNA in genome stability and beyond. *Chem. Rev.* **118**, 4365–4403 (2018).
61. Chipumuro, E. et al. CDK7 inhibition suppresses super-enhancer-linked oncogenic transcription in MYCN-driven cancer. *Cell* **159**, 1126–1139 (2014).
62. Christensen, C. L. et al. Targeting transcriptional addictions in small cell lung cancer with a covalent CDK7 inhibitor. *Cancer Cell* **26**, 909–922 (2014).
63. Di Micco, R. et al. Oncogene-induced senescence is a DNA damage response triggered by DNA hyper-replication. *Nature* **444**, 638–642 (2006).
64. Dimitrova, N., Chen, Y.-C. M., Spector, D. L. & de Lange, T. 53BP1 promotes non-homologous end joining of telomeres by increasing chromatin mobility. *Nature* **456**, 524–528 (2008).
65. Aymard, F. et al. Genome-wide mapping of long-range contacts unveils clustering of DNA double-strand breaks at damaged active genes. *Nat. Struct. Mol. Biol.* **24**, 353–361 (2017).
66. Sun, D., Wu, R., Zheng, J., Li, P. & Yu, L. Polyubiquitin chain-induced p62 phase separation drives autophagic cargo segregation. *Cell Res.* **28**, 405–415 (2018).
67. Bouchard, J. J. et al. Cancer mutations of the tumor suppressor SPOP disrupt the formation of active, phase-separated compartments. *Mol. Cell* **72**, 19–36 (2018).
68. Rulten, S. L. et al. PARP-1 dependent recruitment of the amyotrophic lateral sclerosis-associated protein FUS/TLS to sites of oxidative DNA damage. *Nucleic Acids Res.* **42**, 307–314 (2014).
69. Krishnakumar, R. & Kraus, W. L. PARP-1 regulates chromatin structure and transcription through a KDM5B-dependent pathway. *Mol. Cell* **39**, 736–749 (2010).
70. Kilic, S. et al. Phase separation of 53BP1 determines liquid-like behavior of DNA repair compartments. *EMBO J.* **38**, e101379 (2019).
71. Shin, Y. et al. Liquid nuclear condensates mechanically sense and restructure the genome. *Cell* **175**, 1481–1491 (2018).

Acknowledgements

We thank N. G. Walter and S. Pitchiaya (Single Molecule Analysis Group and Center for RNA Biomedicine, Department of Chemistry, University of Michigan) for the generation of crucial preliminary data; all of the F.d'A.d.F. group members for support and discussions; E. Soutoglou (Institut de Génétique et de Biologie Moléculaire et Cellulaire, Strasbourg, France) and J. Lukas (Novo Nordisk Foundation Center for Protein Research, Copenhagen, Denmark) for reagents; C. Zeirhut (Laboratory of Chromosome and Cell Biology, The Rockefeller University, New York, USA) for reagents and discussions; F. Iannelli for bioinformatic analysis of repair products; S. Pasqualato (Biochemistry and Structural Biology Unit at the European Institute of Oncology IRCCS, Milan, Italy) for the purification of DNA fragments. F.P. was supported by a Marie Curie international mobility fellowship part of Structured International Post Doc Program; F.G. and R.C. were supported by the Regione Lombardia and Cariplo foundation (Project-2016-0998); F.G. was supported by the Associazione Italiana per Ricerca sul Cancro, (MFAG 2018-22083); F.d'A.d.F. was supported by AIRC (application numbers 12971 and 21091), the Cariplo Foundation (grant number 2014-0812), the Fondazione Telethon (GGP17111), PRIN 2010–2011 and 2015, the Italian Ministry of Education Universities and Research EPIGEN Project, InterOmics Project and AMANDA project Accordo Quadro Regione Lombardia-CNR, a European Research Council advanced grant (322726), AriSLA (project 'DDRNA and ALS') and AIRC Special Program 5 per mille metastases (Project-21091).

Author contributions

F.G. conceived and performed all of the LLPS analyses of 53BP1 foci. Y.Y. performed all of the STORM experiments. U.G., together with M.G., performed timelapse experiments of 53BP1 foci treated with NH_4OAc and 1,6-hexanediol, and performed comet assays and the EJ5 repair assays. V.V. conceived and performed strand-specific RT–qPCR and qPCR analysis of ChIP experiments and dilncRNA detection both in cells and in vitro. A.G. conceived and performed DIPLA analysis. S.B. performed all of the microinjections in cells and all of the 53BP1 droplets detection experiments in vitro. M.G. performed all of the timelapse experiments assisted by U.G. F.P. performed all of the FRAP experiments and confocal analysis of 53BP1 focus formation. A.O. performed all of the quantifications of confocal images. A.F. supervised F.P. for the in vitro system and nucleosome preparation and edited the manuscript. R.C. advised F.G. and edited the manuscript. D.P. supervised S.B., M.G. and A.O. and advised them on all of the imaging experiments. E.R. supervised Y.Y. and edited the manuscript. F.P. designed and performed all of the remaining experiments and wrote the manuscript. F.d'A.d.F. conceived the study and, together with F.P., assembled and revised the manuscript. All of the authors commented on the manuscript.

Competing interests

F.d'A.d.F. is listed as an inventor on the patent application: PCT/EP2013/059753.

Additional information

Supplementary information is available for this paper at https://doi.org/10.1038/s41556-019-0392-4.

Correspondence and requests for materials should be addressed to F.d.

Reprints and permissions information is available at www.nature.com/reprints.

Publisher's note Springer Nature remains neutral with regard to jurisdictional claims in published maps and institutional affiliations.

Methods

Cell culture, transfection and IR. Plasmids and Lipofectamine were diluted in different volumes according to the manufacturer's recommendations in OptiMEM (GIBCO) and added to the media in the dish. Cells were used for experiments 24 h after transfection. In the case of transfection in cells treated with siRNA, plasmid was inserted during the final 24 h of recovery after the second round of siRNA addition. U2OS, U2OS 53BP1–GFP[42], HEK293T, HeLa and HeLa ptight 111 cells, a HeLa-derived cell line bearing a LacO-ISceI plasmid[72], were grown under standard tissue culture conditions (37 °C, 5% CO_2) in MEM with Glutamax (GIBCO), supplemented with 10% FBS, 1% non-essential amino acids, 1% sodium pyruvate and 1% penicillin–streptomycin. Where indicated, 10 µg (for a 10 cm dish) of mammalian ER-I-PpoI-expressing plasmid (gift from M. Kastan) or an empty vector control were transfected into HeLa cells, and grown in medium without phenol red. Then, 24 h later, to activate the nuclear translocation of ER-I-PpoI, cells were treated with 4-hydroxytamoxifen (4-OHT) (Sigma-Aldrich) at a final concentration of 2 µM for 4 h. RNA was collected 4 h after induction. IR was induced using a high-voltage X-ray generator tube (CellRad benchtop X-ray irradiator). For the analysis of DDR markers, cells were fixed or lysed at 15 min after IR unless otherwise stated. When stated, cells were treated with 100 µM DRB, 100 nM THZ1, 2 µM ATMi KU-60019, 100 µM mirin, 50 mM NH_4OAc or 0.5–1% 1,6-hexanediol.

ChIP. HeLa ptight 111 cells expressing the inducible I-SceI nuclease were incubated with doxycycline (1 µg ml^{-1}) or mock induced (DMSO) for 16 h before crosslinking. ChIP assays in HeLa cells cut by I-PpoI were performed as described previously[73]. In brief, cells were induced by 4-OHT (Sigma-Aldrich) 4 h before fixation, crosslinked in 1% paraformaldehyde (PFA). Cells were resuspended in buffer A (100 mM Tris-HCl pH 8 and 10 mM dithiothreitol (DTT)) for 15 min at 30 °C, 15 min on ice, 5 min at 4 °C in buffer B (10 mM HEPES pH 7.5, 10 mM EDTA, 0.5 mM EGTA and 0.25% Triton X-100), 5 min at 4 °C in buffer C (10 mM HEPES pH 7.5, 10 mM EDTA, 0.5 mM EGTA and 200 mM NaCl). The cells were finally resuspended in buffer D (50 mM Tris HCl, 10 mM EDTA and 1% SDS) and sonicated with a Bioruptor sonicator to obtain a resolution of 250 bp. Then, 100 µg of chromatin was used per sample for Fig. 1a,b, 40 µg of chromatin was used for ChIP assays performed on samples obtained from cells treated with siRNA.

Standard RT–qPCR and strand-specific RT–qPCR. For standard RT–qPCR, cDNA was generated using the SuperScript VILO reverse transcriptase (Life Technologies). SYBR Green-based RT–qPCR experiments were performed using a Roche LightCycler 480 sequence detection system using Roche SYBR. Ribosomal RNA 7SK was used as a housekeeper reference for normalization.

For DSB-induced transcript detection, chromatin bound RNA was obtained by fractionation from total RNA following a previously published protocol (ref. [74], steps 8–16). After recovery of the chromatin fraction, 50 U of Turbo DNase (Ambion) was added to the pellet and incubated at 37 °C for 10 min, followed by digestion with 200 µg of proteinase K (Roche) at 37 °C for 10 min. RNA was then purified using the Maxwell RSC simplyRNA tissue kit (Promega). Then, 500 ng of total RNA was reverse transcribed using the Superscript First Strand cDNA synthesis kit (Invitrogen) with strand-specific primers. The primers for reverse-transcription that were used for HeLa cells transfected with I-PpoI plasmid were 7SK_R and DAB1 RR 500. For in vitro detection of dilncRNA, Lac-F primers were used for the detection of Lac from dilncRNA[6].

Expression of DSB-induced transcripts in induced (cut) and not induced (uncut) cells was determined by RT–qPCR using Roche SYBR green, EvaGreen Supermix (Bio-Rad) reagent. For each RT–qPCR reaction, 25 ng of cDNA was used. To amplify Lac and Tet repeats, we adapted a technique, as previously described[75], which enables the generation of a fixed-length amplification product.

Immunoprecipitation. HEK293 cells that were irradiated (2 Gy) or not irradiated were collected 10 min after IR and washed in ice cold 1× TBS and resuspended in 0.5 ml of lysis buffer (50 mM Tris pH 7.5, 150 mM NaCl, 0.5% NP-40, 5 mM $MgCl_2$, 5% glycerol, 1× protease inhibitors (Roche tablet) and 1× phosphatase inhibitor tablet (Roche)) supplemented with 1 µl of benzonase (250 U µl^{-1}, Sigma) per 1 ml of lysis buffer. Lysates were incubated at 4 °C for 45 min. Lysates were cleared and equal amounts of total protein extracts were used for each sample. Primary antibodies, preincubated with G Dynabeads (Invitrogen), were added and left at 4 °C on a wheel for a further 2 h. The beads were gently collected using a magnetic rack (Invitrogen) and washed 6 times with 1× lysis buffer and resuspended in 50 µl of sample loading buffer (Invitrogen).

In vitro RNAPII binding to DNA ends. HeLa nuclear extract was prepared according to a modified protocol described previously by Dignam[76]. Nuclear protein extract was incubated with 44% ammonium sulfate with stirring overnight at 4 °C, then centrifuged at 4 °C for 1 h. The supernatant was discarded and the pellet was resuspended in Tris-HCl 7.5 pH, 150 mM NaCl, 1 mM DTT, and protease and phosphatase inhibitors tablets from Roche, to obtain a protein concentration of around 20 mg ml^{-1}. Nuclear protein extract was then dialysed (3,000 molecular weight cut-off) overnight at 4 °C in the same resuspension buffer to remove the ammonium acetate. Then, 100 bp complementary biotinylated oligonucleotides, 50 bp oligonucleotides and 50 bp oligonucleotides with an additional 10 protruding nucleotides were mixed and annealed at room temperature after 5 min incubation at 95 °C. The solutions were incubated with 5 µl streptavidin Dynabeads C1 (Invitrogen) and bound as described previously[77]. Immobilized oligonucleotides were incubated in nuclear extract at 16 °C for 1 h, washed 3 times in 1× TBS and resuspended in sample buffer.

In vitro DDR signalling assay. Biotinylated primers were used to PCR amplify the DNA fragment containing I-SceI and Lac and Tet repeats from the pLac-Tet plasmid containing an I-SceI site flanked by 3× Tet and 8× Lac elements into the pMK-RQ vector (GENEART). The PCR fragment was then purified by ReverseQ column binding and eluted using a salt gradient. Selected fractions were collected, concentrated by ethanol precipitation and resuspended in Tris-EDTA buffer solution. The DNA fragment was mixed with octamers to obtain 100 pmol of nucleosome array and dialysed in 850 mM, 650 mM, 500 mM and 150 mM NaCl buffer. In the case of I-SceI carrying nucleosomes, nucleosomes were bound to beads as described previously[7], an equivalent of 1 µg of DNA (chromatinized) was incubated in I-SceI NEB buffer and subsequently incubated at 37 °C for 1 h in the presence of 1 µl I-SceI enzyme (NEB). Magnetic beads were then washed three times in cold 1× TBS and then incubated at 16 °C with HeLa cells nuclear extract for 80 min. After six washes in cold TBS, beads were boiled in 2× Invitrogen sample buffer and the samples were analysed by western blot. The complete list of primers used is provided in Supplementary Table 1. rNTPs were added to a final concentration of 0.5 mM, 5,6-dichloro-1-β-D-ribofuranosylbenzimidazole (DRB) 100 µM, α-amanitin 50 µg ml^{-1}, RNase A 1 µg µl^{-1}, and anti-TBP, anti-TFIIB and anti-Flag antibodies 4 µg mg^{-1}.

In vitro droplet formation. DNA fragments were chromatinized as described above. U2OS cells expressing 53BP1–GFP were collected by trypsinization, washed in cold 1× TBS, resuspended in hypotonic solution (10 mM HEPES pH 7.9, 1.5 mM $MgCl_2$, 10 mM KCl, 1 mM DTT, and protein and phosphatase tablets from Roche), incubated on ice for 5 min. Then, 0.1% NP-40 was added and cells were incubated on ice for a further 5 min. Cells were centrifuged at 2,000 r.p.m. for 10 min. The supernatant was discarded as the cytosolic fraction, and the pellet (nuclear fraction) was resuspended in two volumes of 20 mM HEPES pH 7.9, 420 mM KCl, 1.5 mM $MgCl_2$, 1 mM DTT, 25% glycerol, and protease and phosphatase tablets from Roche. After a 15 min incubation on ice, the nuclear fraction was cleared by centrifugation at 15,000 r.p.m. at 4 °C, and subsequently precipitated by ammonium sulfate and dialysed as described above. For droplet assays, a MatTek dish with a glass bottom was coated with 1× gelatin (incubated for 1 h and washed with same buffer as protein final resuspension) for Fig. 8a,b. A chamber made by a glass slide and coverslip supported by double tape was coated with a lipid layer as described previously[78] for Fig. 8c,d. Nucleosomes (1 µg of chromatinized DNA), rNTP or total RNA (500 ng) were added simultaneously in 1 mg of nuclear extract (50 µl) and incubated for 30 min at room temperature before microscopy analysis. NH_4OAc (100 mM) or 1,6-hexanediol (1%), THZ1 (100 nM) and ASO (1 µM) treatments were added as indicated. In the case of experiments in which droplets were disrupted, THZ1 (100 nM) or ASOs (1 µM) were added 30 min after droplets were formed and dropped on the bottom of the glass.

RNA interference. The siGENOME smart pool siRNA oligonucleotides (Dharmacon) were transfected at a final concentration of 20 nM by Lipofectamine RNAiMax (Life Technologies) following the manufacturer's protocol. Then, 48 h later, siRNAs were added again and DNA damage was induced 24 h later and samples were collected. A complete list of siRNAs used is provided in Supplementary Table 1.

Indirect immunofluorescence and imaging analysis. HeLa and U2OS cells were fixed in methanol:acetone 1:1 for 2 min at room temperature. For the siTBP and siTFIIB add-back experiment, cells were washed in 1× TBS and fixed in 4% PFA for 10 min at room temperature. Immunofluorescence for DDR markers was performed as described previously[5].

Immunofluorescence images for DIPLA analysis Fig. 2h were acquired in parallel with identical acquisition parameters using a widefield Olympus Biosystems Microscope BX71 and the MetaMorph software (Soft Imaging System). Quantification of the number of nuclear foci per nucleus was performed with the image-analysis software CellProfiler[79] v.3.1.8 in collaboration with senior members of the IFOM Imaging Unit, who performed all of these analyses blinded to treatment. In brief, the DAPI channel was used to identify nuclei and create the nuclear masks. In these areas, foci were identified and their fluorescence intensities were measured. An enhancement filter was applied to focus channels to reduce the background noise and improve focus recognition, although all of the measurements were performed on the original images. For each group of experiments, an intensity threshold, which was evaluated on the foci intensity distribution in the reference sample, was used to identify what in the analysis would be considered to be fully formed foci in a physiological condition. The size of these filtered foci was then measured and, eventually, foci were associated with the 'parent' nucleus to measure the number of foci per cell and the mean of the child object measurements per cell. Only cells entirely in the field were considered for quantification.

For microinjection experiments, an additional intensity threshold was applied on the IgG fluorescence channel to discriminate between microinjected and non-microinjected cells, and measurements were carried out in parallel on both cell populations.

For Fig. 4a–c and Supplementary Fig. 4a–c,f, confocal images were sequentially acquired on a Leica TCS SP8 system using a Leica DMi8 inverted microscope equipped with an HC PL APO CS2 ×63/1.40 NA oil-immersion objective. The samples were illuminated with 405 nm laser line for the excitation of DAPI signal and with a white light laser tuned at 488 nm, 561 nm and 640 nm for the excitation of GFP or AlexaFluor 488, Cy3 and AlexaFluor 647, respectively. The acquisition software used was Leica Application Suite X, v.3.5.2.18963. An image format of $1,024 \times 1,024\ px^2$ was used and an additional ×2 optical zoom was used for sample acquisition, giving a final pixel size of 90 nm.

For Fig. 4c, microinjections were performed using an AIS2 computer-assisted micromanipulation system equipped with a FemtoJet pump (Eppendorf) mounted on an inverted Zeiss microscope with a motorized stage.

The antibodies against TBP or TFIIB were injected in U2OS cell nuclei 20 min after irradiation (1 Gy), and cells were fixed 15 min after injection. U2OS cells for each experiment were microinjected with anti-Flag mouse (M2 F1804 Sigma), anti-Flag goat (NB600-344, Novus Biologicals), anti-TBP mouse (ab51841, Abcam), anti-TBP goat (NBP2-12933 Novus Biologicals) or anti-TFIIB mouse (Abcam ab12094) antibodies. The antibodies were concentrated and dialysed in 50 mM Tris pH 7.4 with 100 mM KCl at a final antibody concentration of $4\ \mu g\ \mu l^{-1}$.

For Fig. 6a,b, FRAP experiments were performed using a Leica TCS SP8 confocal system mounted on a DMi8 microscope and using a HCX PL APO ×63/1.4 NA oil-immersion objective. A 488 nm argon laser was used for both imaging and photobleaching. The FRAP wizard of Leica LAS X was used for each experiment; the parameters were set to use a very low laser power for imaging, an efficient bleaching close to the image background and enough post-bleach timepoints were collected to reach the plateau of the recovery curve or, at least, to calculate it. All of the steps in the analysis were performed using the same software, including background subtraction, correction for imaging photobleaching, normalization, curve fitting (single exponential) and mathematical data collection (recovery half-time and mobile/immobile fraction).

For Fig. 6c,d, time-lapse confocal microscopy was performed using a UltraVIEW VoX spinning-disk confocal system (PerkinElmer) mounted on an Eclipse Ti inverted microscope (Nikon) equipped with a Nikon Perfect Focus System, Nikon Plan Apo TIRF ×60/1.40 NA oil-immersion objective and a Hamamatsu EM-CCD camera (C9100-50). Live-cell conditions were achieved using an incubation chamber (OKOLab) maintained at 37 °C in an atmosphere of 5% CO_2. Volocity software (Perkin Elmer) was used to manage the system. A single plane was acquired at maximum speed, limited only by the camera exposure time (400 ms). At specific timepoints, treatment and wash-out were applied without interrupting the acquisition. Cells were imaged using a 488 laser line using the lowest power possible, considering both cell viability and signal-to-noise ratio. 53BP1–GFP-expressing U2OS cells were seeded onto 28 mm glass coverslips or onto 35 mm MatTek dishes and irradiated. Cells were then time-lapse imaged 30 min after IR. NH_4OAc or 1,6-hexanediol was added to the cells during time-lapse imaging to a final concentration of 50 mM or 1%, respectively. For the wash-out experiment in Fig. 6d, 50–60 s after NH_4OAc addition, fresh culture medium was added to cells to reduce the concentration of NH_4OAc to 10 mM.

For Fig. 7a,b, time-lapse confocal microscopy was performed using a UltraVIEW VoX spinning-disk confocal system (PerkinElmer) mounted on an Eclipse Ti inverted microscope (Nikon) equipped with a Nikon Perfect Focus System, Nikon Apo TIRF ×100/1.49 NA oil-immersion objective and a Hamamatsu EM-CCD camera (C9100-50). Live-cell conditions were achieved using an incubation chamber (OKOLab) maintained at 37 °C in an atmosphere of 5% CO_2. Volocity software (Perkin Elmer) was used to manage the system. z-stacks (6 slices with 1 µm z-step) of multiple positions were acquired every 1 min during the first hour, every 3 min during the second hour and every 5 min until the end of the time lapse (12 h). The cells were imaged using a 488 laser line using the lowest power possible, considering both cell viability and signal-to-noise ratio.

For Fig. 8a,b, images were acquired with a spinning-disk confocal microscope (Olympus) equipped with an IXON 897 Ultra camera (Andor) and a FRAP module furnished with a 405 nm laser, using a ×60/1.35 NA objective.

For Fig. 8c,d, droplets were acquired using a DV Elite system (GE Healthcare) equipped with a IX71 microscope (Olympus) and a sCMOS camera and driven by softWoRx v.7.0.0. We used a ×100 UPlanSApo 1.40 NA objective.

For Fig. 8f, the microinjections experiments were performed using an UltraVIEW VoX spinning-disk confocal system (PerkinElmer) driven by Volocity software v.6.3.1 (Improvision; Perkin Elmer) and equipped with an EclipseTi inverted microscope (Nikon) provided with a Yokogawa CSU-X1 confocal scanner unit, a Hamamatsu CCD camera (C9100-50) and a motorized Luigs & Neumann SM7 micromanipulator.

Glass borosilicate capillaries (Harvard Apparatus) were pulled to a final diameter of 0.7 µm using a P1000 puller (Sutter Instrument) and loaded with ASOs or control solution containing DAPI as an injection marker.

The material was injected into the cell nucleus using a FemtoJet pump (Eppendorf) to maintain a constant pressure of 40 hPa.

After injection, cells were immediately monitored for 1 h 30 min, and a z-stack was acquired (6 stacks, 1 µm spacing) every 5 min.

All of the images were acquired through a ×60 oil-immersion objective (Nikon Plan Apo VC, 1.4 NA); 405 nm, 488 nm and 561 nm lasers were used to excite DAPI, GFP and mCherry, respectively.

Intensity correlation analysis of droplet shape fluctuations. Regions of interest (ROIs), including single foci, were manually selected from sequences of confocal images (effective pixel size, 0.09 µm; delay between frames, 0.1 s). Typical ROI size was $50 \times 50\ px^2$. In total, 52 ROIs that were obtained from 25 nuclei over 13 image sequences of 600 frames each were considered. For each ROI, a registered image stack $I(x, t)$ was obtained by applying the following procedure to each frame:

(1) Low-pass filtering (with a Gaussian filter of width of 1 px) to reduce noise.
(2) Thresholding, leading to a binary image of the focus.
(3) Registration (using the imregister MATLAB function) to minimize global rototranslational motion with respect to the previous (registered) frame.

From the stack obtained as described above, we calculated the intensity structure function (ISF) as: $d(\Delta t) = \left\langle \sum_{\mathbf{x}} [I(\mathbf{x}, t_0 + \Delta t) - I(\mathbf{x}, t_0)]^2 \right\rangle$ where $\langle\cdot\rangle$ indicates an average performed over all initial times t_0 and the sum is performed over all pixel positions $\mathbf{x}$. $d(\Delta t)$ typically displays a rapid increase followed by a slower, approximately linear, drift. As the overall motion of the focus was removed in the preprocessing steps, we interpreted the rapid decorrelation of d as being due to random shape changes, which occur with a characteristic relaxation time $\tau < 2$ s. The long-time drift is mainly due to photobleaching, which systematically lowers the total intensity in the image. A linear fit $h(t) = a + bt$ of $d(\Delta t)$ for large delay times ($3\ s < \Delta t < 10\ s$) enabled the capture and effective removal of this spurious effect from the ISF. We indicate with $d'(\Delta t)$ the corrected ISF, in which the linear drift has been subtracted. To estimate the characteristic correlation time τ, we fitted $d'(\Delta t)$ with an exponential function of the form $f(t) = A(1 - e^{-t/\tau}) + B$. The size R of the focus was estimated according to the following procedure. We projected the time-averaged intensity map $\langle I(\mathbf{x}, t_0)\rangle$ along the vertical and the horizontal direction, obtaining the profiles $V(y)$ and $H(x)$, respectively. A fit of V and H with a Gaussian function $g(x) = ae^{-(x-x_0)^2/\sigma^2}$ provided an estimate of their widths σ_V and σ_H, respectively. R is calculated as the sum in quadrature of σ_V and σ_H.

A plot of the characteristic relaxation time τ as a function of the size R is shown in Fig. 7d for all of the analysed foci. The relationship between τ and R is compatible with a linear dependence (Pearson coefficient of linear correlation $R_p \approx 0.44$, $P \approx 0.001$). A best fit to the data with a linear homogeneous function $\tau = cR$ provides $c = 1.0 \pm 0.1\ s\ \mu m^{-1}$.

Fourier analysis of droplet shape fluctuations. Regions of interest (ROIs) including single foci were manually selected from sequences of confocal images (effective pixel size, 0.09 µm; delay between frames, 0.1 s). For each ROI, the corresponding image sequence was filtered and registered as described in the previous section to obtain a registered stack $I(\mathbf{x},t)$. Fourier-domain analysis was performed on 15 of the 52 ROIs considered in previous section, corresponding to the larger droplets ($R > 2$ µm).

From the registered stack $I(\mathbf{x},t)$, we first calculated the average intensity map $I_m(\mathbf{x}) = \langle I(\mathbf{x},t_0)\rangle$ from which, using the MATLAB function bwboundaries, we obtained a curve $\mathbf{x}(s)$ that describes the average contour of the focus. Here $\mathbf{x}$ represents the pixel coordinates and s is a curvilinear abscissa spanning the interval $[0, L]$ where L is the perimeter of the focus. For each frame, we extracted the boundary spatiotemporal profile as $B(s,t) = I(\mathbf{x},t) - I_m(\mathbf{x})_{U[\mathbf{x}(s)]}$ where $\langle\cdot\rangle_{U[\mathbf{x}]}$ indicates the spatial average performed over a small square domain with a linear size of 5 px centred on $\mathbf{x}$. We studied the spatiotemporal fluctuation of B in the Fourier domain by considering the q-dependent intensity structure function $\left(D(q, \Delta t) = \left\langle \left|\hat{B}(q, t_0 + \Delta t) - \hat{B}(q, t_0)\right|^2 \right\rangle_{t_0}\right)$. This function is the one-dimensional analogue of the image structure function used in differential dynamic microscopy to measure the dynamics of intensity fluctuation in the Fourier space[80,81]. Here $\hat{B}(q, t_0)$ indicates the spatial Fourier transformation of $B(s,t_0)$. For the lowest q values, D displays a well-defined relaxation towards a plateau value, whereas for $q \geq 5q_0$ where the ISF $q_0 = \frac{2\pi}{L}$ is typically too noisy to discern any meaningful trend.

A q-dependent relaxation rate $\Gamma(q)$ is obtained by fitting $D(q,\Delta t)$ for fixed $q < 5q_0$ with an exponential function of the form: $a(q)[1 - \exp(-\Gamma(q)\ \Delta t)] + b(q)$. For most of the analysed foci, $\Gamma(q)$ is found to be an increasing function of q, which is well described by a linear function. A best fit to the data with a linear homogeneous function $\Gamma(q) = v_0 q$ provides an estimate of the proportionality constant v_0. By averaging over the 15 analysed foci, we found that $v_0 = 0.25 \pm 0.5\ s\ \mu m^{-1}$.

Estimation of the foci internal viscosity. An estimate of the internal viscosity η was obtained from FRAP experiments according to the following procedure. A small region (of width $w \approx 0.35 \pm 0.05$ µm) within a larger focus was photobleached (Fig. 6b). w was estimated from a Gaussian fit of the intensity profile immediately after photobleaching. A fit of the fluorescence recovery curve with an exponential function enabled measurement of the recovery time τ, from which we obtained an order of magnitude estimate of the diffusion coefficient of the fluorescently

tagged protein within the focus as $D_0 \approx \frac{w^2}{\tau}$. We estimated the hydrodynamic radius of the tagged protein by means of the empirical formula $R \approx 0.475\, N_R^{0.29}$ where $N_R \approx 2{,}000$ is the number of residuals and R is expressed in nm as described previously[82]. We obtained $R \approx 4.3$ nm. For a given focus, we obtain an estimate of the internal viscosity by means of the Stokes–Einstein relation: $\eta = \frac{kT}{6\pi R D_0}$ where k is the Boltzmann constant and $T \approx 310$ °K is the absolute temperature. We repeated the above procedure at 1 h, 4 h and 8 h after IR. In each case, a number n of foci of between 8 and 14 was considered. The measured recovery times, expressed as mean ± s.e.m. were $\tau_1 = 4.9 \pm 1s$, $\tau_4 = 6.6 \pm 1s$ and $\tau_8 = 10 \pm 2$ s, respectively, leading to the following values for the internal viscosity $\eta_1 = 1.9$ Pa s, $\eta_4 = 2.5$ Pa s and $\eta_8 = 4.1$ Pa s, respectively. Given the substantial approximations leading to these estimates, the associated uncertainty is very large (a factor of two, roughly). Nevertheless, this uncertainty is mainly systematic in nature (that is, associated with an undetermined constant prefactor) and does not significantly affect the relative increment of the foci internal viscosity over time, which can be reliably quantified in about 30% (100%) from 1 h to 4–8 h.

53BP1–GFP liquefaction analysis. During each experiment, a dual-channel (green (G) and red (R)) sequence of three-dimensional (3D) image stacks (512×512×7) was acquired. Voxel size was 0.21 µm×0.21 µm×1 µm and the delay time between consecutive stacks was 30 s. Let $I_R(x,y,z|t)$ and $I_G(x,y,z|t)$ be the intensity recorded in voxel (x,y,z) at time t in the red (mCherry) and in the green (GFP) channel, respectively.

The 3D position of the damage site at a given time t_0 is identified as the point of coordinates (x_M,y_M,z_M) where the intensity of the 3D stack $I_R(x,y,z|t_0)$ has a maximum. Size and average intensity of the focus were estimated by considering the intensity distribution in the green channel across the z_M plane. In particular, the one-dimensional sections $f_x(x|t_0) = I_G(x,y_M,z_M|t_0)$ and $f_y(y|t_0) = I_G(x_M,y,z_M|t_0)$ were considered. By fitting f_x with a Gaussian function: $A_x e^{-(x-x_0)/2\sigma_x^2} + I_0$ we obtained an estimate of the intensity A_x and of the linear extension σ_x of the focus along the x axis. An identical procedure leads to the analogous quantities A_y and σ_y obtained in the perpendicular direction. Finally, focus volume $V(t_0)$ and average intensity $i(t_0)$ are calculated, respectively, as $V(t_0) = \left[\left(\sigma_x^2 + \sigma_y^2\right)/2 - \sigma_0^2\right]^{3/2}$ and $i(t_0) = (A_x + A_y)/2$. In the expression $V(t_0)$, a correction term is included to account for the spreading in the image of the foci due to diffraction. Here $\sigma_0 \approx 0.4$ µm is the theoretical RMS lateral width of the optical point spread function of the microscope. In treated cells, we observed a decrease in both average intensity and volume with distinct characteristic timescales. In control cells, average intensity and volume do not show any significant trend during the observation window (30 min).

An estimate of the characteristic timescales τ_V associated with the evolution of focus volume over time is obtained by fitting $V(t)$ with a simple exponential model $(Ae^{-t/\tau V} + B)$. A similar fitting procedure provides the characteristic decay time τ_i of the average intensity.

The fact that the focus average intensity does not change over time in control cells indicates that bleaching can be safely neglected and that the observed decay in the average intensity in treated cells can be attributed to a change in the local concentration of 53BP1–GFP.

STORM super-resolution analysis. *Cell culture, NCS treatment and EU labelling.* The U2OS cell lines (ATCC, HTB-96) were cultured in DMEM medium (Thermo Fisher, 11965) with 10% FBS (Gemini, 100-106) and 100 U ml^{-1} penicillin–streptomycin (Thermo Fisher, 15140). For STORM imaging, cells were seeded on glass coverslips and were allowed to establish for 24–48 h. The cells were then mock treated or treated with 100 ng ml^{-1} NCS for 30 min and, during the last 15 min of which, the cells were pulse treated with 0.5 mM EU.

Cell extraction, fixation and fluorescent labelling. Fixation and immunofluorescence labelling of nuclei was carried out following established protocols for extraction and fine removal of proteins that are unbound to chromatin[83]. After EU labelling, cells were immediately treated with 0.5% Triton X-100 in CSK buffer (10 mM HEPES, 300 mM sucrose, 100 mM NaCl, 3 mM $MgCl_2$, pH 7.4) for 10 min and fixed with PFA (4%) for 30 min. After two washes with 1 ml blocking buffer for 5 min (2% glycine, 2% BSA, 0.2% gelatin and 50 mM NH_4Cl in PBS), EU was tagged with Alexa Fluor 488 picolyl azide through the click reaction. The cells were blocked with blocking buffer for 1 h at room temperature or overnight at 4 °C for immunofluorescence staining with the indicated antibodies. The fixed cells were then mounted onto microscope glass for single-molecule localization microscopy (SMLM) based super resolution (SR) imaging in freshly mixed imaging buffer (1 mg ml^{-1} glucose oxidase, 0.02 mg ml^{-1} catalase, 10% glucose and 100 mM cysteamine).

Microscope setup, STORM imaging and single-molecule reconstruction. STORM imaging was performed using a custom-built optical imaging platform based on a Leica DMI 300 inverse microscope. γH2AX was tagged with Alexa Fluor 647, which was excited using a 639 nm laser (UltraLaser, MRL-FN-639-800). POL2, TBP and CDK7 were tagged with Alexa Fluor 568, which was excited using a 561 nm laser (UltraLaser, MGL-FN-561-200). EU was tagged with Alexa Fluor 488, which was excited using a 488 nm Laser (OBIS). These laser lines were aligned, collimated and reflected into an HCX PL APO ×63/1.47 NA OIL CORR TIRF objective (Zeiss) by a penta-edged dichroic beam splitter (FF408/504/581/667/762-Di01-22x29). The 488, 561 and 639 nm laser lines were adjusted to approximately 0.8, 1.0 and 1.5 kW cm^{-2}, respectively. The illumination was adjusted to the highly inclined and laminated optical sheet (HILO) mode for nucleus imaging. A 405 nm laser line (Allied Scientific Pro, SL 405 nm, 300 mW) was also introduced to drive Alexa Fluor 647 fluorophores back to their ground state.

The emitted fluorescence of different colours was further expanded using a ×2 lens tube and filtered using a single-band-pass filter accordingly (Alexa Fluor 647: FF01-676/37, Semrock; Alexa Fluor 568: FF01-607/36, Semrock; Alexa Fluor 488: FF01-531/40, Semrock). Different colours were collected by sequentially switching the laser and the single-band-pass filter accordingly in a filter wheel (ThorLabs, FW102C). The photons were then recorded using a sCMOS camera (Photometrics, Prime 95B). All of the raw image stacks of different colours were acquired at 33 Hz for 2,000 frames.

The single-molecule reconstruction was carried out following a maximum-likelihood estimation fitting of each single point spread function (PSF)[84]. In brief, the probability of the number of photons recorded on each camera pixel was moulded by the Poisson distribution convolved by a Gaussian-modelled camera read-out noise, which was precalibrated[13]. The likelihood function at each pixel was then fitted by satisfying the maximum likelihood criteria through the Gauss–Newton convergence. The fitting accuracy was also estimated by the Cramér–Rao lower bound, and the distribution of the accuracy of all of the successive localizations were fitted into a skew Gaussian distribution, the centre of which was used to present the localization accuracy. Furthermore, the localizations that appeared in consecutive frames within 2.5× of the localization precision were considered to be one blinking event for the purpose of computation of auto-pair correlation (Auto-PC)[85].

Alignment of images of different colours. Mapping among different channels was performed using a polynomial morph-type mapping algorithm. The map was generated by acquiring diffraction-limited images of spatially separated fluorescent beads (Thermo Fisher, T-7279), which emitted fluorescence spanning a broad range covering all of the three-colour channels utilized in this study. The localizations of the beads were obtained by fitting their PSF with a two-dimensional Gaussian function. The localizations of the beads in the red channel were then submitted as the reference, and those of the same beads in the green and blue channels were fitted to match the reference localizations using a second polynomial function. The optimized functions were used to map the green and blue STORM images onto the red STORM images for experimental sets.

Cross-pair correlation. Computation of the cross-pair correlation was performed as previously described[14]. As for cross-pair correlation analyses, a 6×6 µm^2 square at the centre of each STORM-imaged nucleus was submitted to the Auto-PC function. As discussed above, the artificial blinking events (one blinking event recorded multiple times in consecutive frames) were eliminated before the computation of cross-pair correlations. The correlation profile was plotted as a function of pairwise distances between the two submitted species, and fitted into a Gaussian model of which the amplitude was recorded as the level of cross-pair correlation of the two species within the submitted STORM image. As for the RND-control, we submitted one species from a 6×6 µm^2 square and the other species from another 6×6 µm^2 square, such that the examined two species from two nuclei should be completely spatially uncorrelated and, therefore, served as the baseline of the level of cross-pair correlation. The unpaired t-test between the experimental set and such randomized set (RND-control) demonstrates the significance of the level of cross-pair correlation of the experimental set.

For the occurrence of colocalization, we multiplied the cross-pair correlation with the image density of the two examined species, and plotted the result as a function of the image density of γH2AX so that we could examine whether the total colocalization occurrence was positively correlated to the damage level (Supplementary Fig. 2). Note that the image density of each species was determined by their Auto-PC analysis[35], in which the multi-blinking-induced overcounting of fluorophores was eliminated.

DBSCAN clustering analysis. Details of the DBSCAN clustering analysis are provided in Supplementary Fig. 6.

DNA-damage repair analysis. Neutral comet assays and non-homologous end joining repair analyses were performed as described previously[7].

Antibodies. Antibodies against the following targets were used in this study: TFIIA, TFIIA1 (rabbit, Bethyl, A302-777A; 1:1,000); TFIIB, (mouse, Abcam, ab12094; 1:1,000); TFIID, TBP (mouse, Abcam, ab51841; 1:1,000); TFIIE, TFIIE1 (rabbit, Abcam, ab28177; 1:1,000); TFIIF, TFIIF1 (rabbit, Abcam, ab28179; 1:1,000); TFIIH, CDK7 (ChIP and western blot rabbit, Bethyl, A300-405A; 1:1,000); MED, MED1 (mouse, Millipore, 17-10530; 1:1,000); CDK9 (rabbit, Abcam, ab6544; 1:1,000); RNAPI, POLR1A (mouse, Santa Cruz, sc-48385; 1:1,000); RNAPII, POLR2A-pSer5 (mouse, Abcam, ab5408; 1:1,000); ChIP analysis total POLR2A (mouse, Abcam, ab817; 1:1,000); immunoblot total POLR2A (mouse, Santa Cruz, 8WG16; 1:100); RNAPIII, POLR3A (rabbit, Novus Biologicals, NBP1-53051; 1:1,000); ATM (mouse,

Sigma-Aldrich, A1106; 1:1,000); pATM, ATM-pS1981 (mouse, Millipore, 05-740, clone 10H11.E12; 1:1,000); MDC1 (mouse, Sigma-Aldrich, M2444; 1:1,000); 53BP1 (rabbit, Novus Biologicals, NB100-304; 1:1,000); MRE11 (rabbit, polyclonal raised against recombinant MRE11, gift from S. P. Jackson; 1:1,000); RAD50 (Millipore, 13B3/2C6, 05-525; 1:1,000); NBS1 (rabbit, Novus Biologicals, NB100-143; 1:1,000); γH2AX, pS139 (mouse, Millipore 05-636; 1:1,000); pS139 (rabbit, Abcam, ab2893; 1:1,000); and H4, histone H4 (rabbit, Abcam, ab10158; 1:1,000).

Details for the antibodies used for the STORM analyses are provided in Supplementary Table 3.

Statistics and reproducibility. Results are shown as mean and the error bars represent the s.e.m. unless stated otherwise. The number of times experiments were repeated with similar results and the number *n* from which statistics are calculated are provided in the figure legend for each experiment. Prism was used to generate graphs and to perform statistical analysis, except for STORM data and LLPS analysis. All of the LLPS analyses in Figs. 6b (i–iv) and 7a–f were performed using MATLAB. *P* values were calculated using one-way ANOVA or parametric *t*-tests, *P* values for linear fitting is the *F*-test against the hypothesis of the slope = 0. *P* values of statistical significance are indicated as NS, $P > 0.05$; $^{*}P < 0.05$; $^{**}P < 0.01$; $^{***}P < 0.001$; $^{****}P < 0.0001$. Experiments shown in Figs. 2d, 3c, 4b, 5b–d, 6a,b, 7a–c and 8a,b, Supplementary Figs. 1b (3,000 bp upstream dataset only), e, 3a and 4a–c,f were been performed twice with similar results. Experiments shown in Figs. 4a,b (−IR dataset only) c, 5e, 8c,d, Supplementary Figs. 1a,b (10,000 bp upstream dataset only), 3b (dilncRNA synthesis in siTFIIB knockdown dataset only) and c (siLuc + TBP–GFP and siLuc + TFIIB–GFP datasets only) were performed once.

Reporting Summary. Further information on research design is available in the Nature Research Reporting Summary linked to this article.

Data availability

All unprocessed blots are shown in Supplementary Fig. 6 and all numerical data used to generate graphs in the manuscript for Figs. 1–8 and Supplementary Figs. 1–6 are provided in Supplementary Table 2. All other information is available from the corresponding author on reasonable request.

Code availability

All code used in this study is available from the corresponding author on reasonable request.

References

72. Lemaitre, C. et al. Nuclear position dictates DNA repair pathway choice. *Genes Dev.* **28**, 2450–2463 (2014).
73. Berkovich, E., Monnat, R. J. Jr & Kastan, M. B. Roles of ATM and NBS1 in chromatin structure modulation and DNA double-strand break repair. *Nat. Cell Biol.* **9**, 683–690 (2007).
74. Nojima, T., Gomes, T., Carmo-Fonseca, M. & Proudfoot, N. J. Mammalian NET-seq analysis defines nascent RNA profiles and associated RNA processing genome-wide. *Nat. Protoc.* **11**, 413–428 (2016).
75. Cawthon, R. M. Telomere measurement by quantitative PCR. *Nucleic Acids Res.* **30**, e47 (2002).
76. M. F. Carey, C. L. Peterson & S. T. Smale, Dignam and Roeder nuclear extract preparation. *Cold Spring Harb. Protoc.* https://doi.org/10.1101/pdb.prot5330 (2009).
77. Zierhut, C., Jenness, C., Kimura, H. & Funabiki, H. Nucleosomal regulation of chromatin composition and nuclear assembly revealed by histone depletion. *Nat. Struct. Mol. Biol.* **21**, 617–625 (2014).
78. Alberti, S. et al. A user's guide for phase separation assays with purified proteins. *J. Mol. Biol.* **430**, 4806–4820 (2018).
79. Carpenter, A. E. et al. CellProfiler: image analysis software for identifying and quantifying cell phenotypes. *Genome Biol.* **7**, R100 (2006).
80. Cerbino, R. & Trappe, V. Differential dynamic microscopy: probing wave vector dependent dynamics with a microscope. *Phys. Rev. Lett.* **100**, 188102 (2008).
81. Giavazzi, F., Brogioli, D., Trappe, V., Bellini, T. & Cerbino, R. Scattering information obtained by optical microscopy: differential dynamic microscopy and beyond. *Phys. Rev. E* **80**, 031403 (2009).
82. Wilkins, D. K. et al. Hydrodynamic radii of native and denatured proteins measured by pulse field gradient NMR techniques. *Biochemistry* **38**, 16424–16431 (1999).
83. Cseresnyes, Z., Schwarz, U. & Green, C. M. Analysis of replication factories in human cells by super-resolution light microscopy. *BMC Cell Biol.* **10**, 88 (2009).
84. Huang, F. et al. Video-rate nanoscopy using sCMOS camera-specific single-molecule localization algorithms. *Nat. Methods* **10**, 653–658 (2013).
85. Veatch, S. L. et al. Correlation functions quantify super-resolution images and estimate apparent clustering due to over-counting. *PLoS ONE* **7**, e31457 (2012).

nature research

Corresponding author(s): Fabrizio d'Adda di Fagagna

Last updated by author(s): Aug 6, 2019

Reporting Summary

Nature Research wishes to improve the reproducibility of the work that we publish. This form provides structure for consistency and transparency in reporting. For further information on Nature Research policies, see Authors & Referees and the Editorial Policy Checklist.

Statistics

For all statistical analyses, confirm that the following items are present in the figure legend, table legend, main text, or Methods section.

n/a	Confirmed	
☐	☒	The exact sample size (*n*) for each experimental group/condition, given as a discrete number and unit of measurement
☐	☒	A statement on whether measurements were taken from distinct samples or whether the same sample was measured repeatedly
☐	☒	The statistical test(s) used AND whether they are one- or two-sided *Only common tests should be described solely by name; describe more complex techniques in the Methods section.*
☐	☒	A description of all covariates tested
☐	☒	A description of any assumptions or corrections, such as tests of normality and adjustment for multiple comparisons
☐	☒	A full description of the statistical parameters including central tendency (e.g. means) or other basic estimates (e.g. regression coefficient) AND variation (e.g. standard deviation) or associated estimates of uncertainty (e.g. confidence intervals)
☐	☒	For null hypothesis testing, the test statistic (e.g. *F*, *t*, *r*) with confidence intervals, effect sizes, degrees of freedom and *P* value noted *Give P values as exact values whenever suitable.*
☒	☐	For Bayesian analysis, information on the choice of priors and Markov chain Monte Carlo settings
☒	☐	For hierarchical and complex designs, identification of the appropriate level for tests and full reporting of outcomes
☐	☒	Estimates of effect sizes (e.g. Cohen's *d*, Pearson's *r*), indicating how they were calculated

Our web collection on statistics for biologists contains articles on many of the points above.

Software and code

Policy information about availability of computer code

Data collection	Super-Resolution Images was collected using ImageJ Micro-Manager which managed the sCMOS acquisition as described in the Method section Spinning disk Perkin Elmer—> Volocity 6.4.0 SP8 confocal —> Leica Application Suite X, version 3.5.2.18963 (usato sia per acquisizione che analisi della FRAP) Spinning disk CSU —> Olympus cellSens Dimension 1.18 (Build 16686) Delta Vision —> softWoRx 7.0.0 Release RC6
Data analysis	Pair-Correlation analyses (including randomization analyses) of Super-Resolution images were accomplished using custom-written Matlab code, which can be found on https://github.com/yiny02/direct-Triple-Correlation-Algorithm Biophysics analysis were made using a custom MATLAB codes that will be made available upon request to qualified researchers Graphs and statistical tests were carried out with Prism software V 8.1 Quantification of foci from confocal images were carried out with CellProfiler Software 3.1.8

For manuscripts utilizing custom algorithms or software that are central to the research but not yet described in published literature, software must be made available to editors/reviewers. We strongly encourage code deposition in a community repository (e.g. GitHub). See the Nature Research guidelines for submitting code & software for further information.

Data

Policy information about availability of data

All manuscripts must include a data availability statement. This statement should provide the following information, where applicable:

- Accession codes, unique identifiers, or web links for publicly available datasets
- A list of figures that have associated raw data
- A description of any restrictions on data availability

No datasets were generated or analysed during the current study. All raw data associated to Figures in manuscript are provided as supplementary material or available upon reasonable request.

Field-specific reporting

Please select the one below that is the best fit for your research. If you are not sure, read the appropriate sections before making your selection.

☒ Life sciences ☐ Behavioural & social sciences ☐ Ecological, evolutionary & environmental sciences

For a reference copy of the document with all sections, see nature.com/documents/nr-reporting-summary-flat.pdf

Life sciences study design

All studies must disclose on these points even when the disclosure is negative.

Sample size	For super-resolution the sample size was determined basing on previous experiences on the standard deviation of correlation analyses. The sample size as shown in the manuscript displays clear standard deviation of its distribution. For other experiments sample size was not pre-determined, as much data as possible was collected depending on the nature of the experiments or in order to have statistical analysis
Data exclusions	No Data exclusions were applied
Replication	For super-resolution analysis at least 3 experimental replicates were performed. RND-ctrl correlation between MCM6 and gH2AX has been performed twice. For the in vitro system it has to be noted that it is technically very challenging and it is not trivial to have all controls working robustly. The quality of the nucleosome preparation, the quality of the extract, the immobilization efficiency of the biotin to the beads they all concur to high variability. We took in consideration only the experiments where all internal controls gave results in accordance to what is known in literature. For the rest of the experiments 3 independent replicates were performed unless differently stated in the figure legends.
Randomization	Nuclei on coverslips were randomly picked for Super-Resolution imaging. Fields for immunofluorescence analysis are picked randomly. For all other studies no randomization is required as a proper and better control is present.
Blinding	Images in Fig4 and S4, Fig8a-d were acquired blind from numerically labelled coverslips. For Super-Resolution imaging blinding is not necessary. The investigators could not tell the difference amongst different experimental groups during data collection because of the stochastic switching of fluorophores. For all other experiments blinding was not applied since internal controls are present and/or were analyzed by unbiased softwares.

Reporting for specific materials, systems and methods

We require information from authors about some types of materials, experimental systems and methods used in many studies. Here, indicate whether each material, system or method listed is relevant to your study. If you are not sure if a list item applies to your research, read the appropriate section before selecting a response.

Materials & experimental systems

n/a	Involved in the study
☐	☒ Antibodies
☐	☒ Eukaryotic cell lines
☒	☐ Palaeontology
☒	☐ Animals and other organisms
☒	☐ Human research participants
☒	☐ Clinical data

Methods

n/a	Involved in the study
☒	☐ ChIP-seq
☒	☐ Flow cytometry
☒	☐ MRI-based neuroimaging

Antibodies

Antibodies used

TFIIA – TFIIA1 (rabbit Bethyl A302-777A 1:1000)
TFIIB – (mouse Abcam ab12094 1:1000)
TFIID – TBP (mouse Abcam ab51841 1:1000)
TFIIE – TFIIE1 (rabbit Abcam Ab28177 1:1000)
TFIIF – TFIIF1 (rabbit Abcam Ab28179 1:1000)
TFIIH –CDK7 (ChIP and WB rabbit Bethyl A300-405A 1:1000, mouse, Santa Cruz Biotechnology sc-7344 1:200)
MED – MED1 (mouse Millipore 17-10530 1:1000)
CDK9 – (rabbit Abcam Ab6544 1:1000)
RNAPI – POLR1A (mouse Santa Cruz sc-48385 1:1000)
RNAPII – POLR2A pSer5 (mouse, Abcam ab5408, 1:1000) – ChIP analysis total POLR2A (mouse, Abcam, ab817 1:1000) – immunoblot total POLR2A (mouse, Santa Cruz 8WG16 1:100)
RNAPIII POLR3A (rabbit Novus Biologicals NBP1-53051 1:1000)
ATM – (mouse Sigma-Aldrich A1106 1:1000)
pATM – ATM-pS1981 (mouse Millipore 05-740 clone 10H11.E12 1:1000)
MDC1 – (mouse Sigma-Aldrich M2444 1:1000)
53BP1 - (rabbit, Novus Biologicals NB100-304, 1:1000)
MRE11 - (rabbit polyclonal raised against recombinant MRE11, kind gift from S. P. Jackson 1:1000)
RAD50 - (Millipore (13B3/2C6) 05-525 1:1000)
NBS1 - (rabbit, Novus Biologicals NB100-143 1:1000)
H2AX - pS139 (mouse, Millipore 05-636, 1:1000) - pS139 (rabbit, Abcam ab2893 1:1000)
H4 – Histone H4 (rabbit Abcam ab10158 1:1000)
MCM6 - (rabbit Abcam ab211916 1:1000)
if not stated otherwise the same antibody and dilution was used for different techniques.

for STORM analysis
γH2AX , ms to γH2AX AF647 conjugated , 05-636-AF647, Millipore 1/10000
RNAPII-pS5, ms to RNAPII-pS5, Ab5408, Abcam 1/1000
TBP, ms to TBP Ab51841, Abcam 1/1000
CDK7, ms to Cdk7, Sc-7344, scbt 1/200

Validation

All antibodies were validated by the manufacturer and were previously used in peer reviewed works. Methods of validation and references to published application for all antibodies are all present into manufacturer dedicated website page of each indicated product.

Eukaryotic cell lines

Policy information about cell lines

Cell line source(s)

HeLa111 cells (Lemaitre et al 2014)
HeLa cells, U2OS cells, HEK293T (ATCC), U2OS 53BP1-GFP (Bekker-Jensen et al. 2005)

Authentication

cell lines are authenticated by STR profiling (StemElite ID system, Promega)

Mycoplasma contamination

all cell lines tested negative for mycoplasma

Commonly misidentified lines
(See ICLAC register)

no commonly misidentified lines were used